



HAL
open science

Precipitation of cerianite crystals and its effect on the rheology of a simplified nuclear glass melt

Jeanini Jiusti, Elise Regnier, Norma Maria Machado, Vincent Malivert,
Muriel Neyret, François Faure

► To cite this version:

Jeanini Jiusti, Elise Regnier, Norma Maria Machado, Vincent Malivert, Muriel Neyret, et al.. Precipitation of cerianite crystals and its effect on the rheology of a simplified nuclear glass melt. International Journal of Applied Glass Science, 2023, 14 (4), pp.502-521. 10.1111/ijag.16639 . cea-04244547

HAL Id: cea-04244547

<https://cea.hal.science/cea-04244547v1>

Submitted on 16 Oct 2023

HAL is a multi-disciplinary open access archive for the deposit and dissemination of scientific research documents, whether they are published or not. The documents may come from teaching and research institutions in France or abroad, or from public or private research centers.

L'archive ouverte pluridisciplinaire **HAL**, est destinée au dépôt et à la diffusion de documents scientifiques de niveau recherche, publiés ou non, émanant des établissements d'enseignement et de recherche français ou étrangers, des laboratoires publics ou privés.

Author Query Form

Journal IJAG

Article ijag16639

Dear Author,

During the copyediting of your manuscript the following queries arose.

Please refer to the query reference callout numbers in the page proofs and respond.

Please remember illegible or unclear comments and corrections may delay publication.

Many thanks for your assistance.

Query No.	Description	Remarks
Q1	Please spell out the first names of all the authors in the author byline.	
Q2	Please check both the affiliations for correctness and provide the department name for affiliation number 2.	
Q3	Please provide the date and month, and city of the proceeding for reference number 2.	
Q4	Please provide the publisher/organization name and its location, or journal title, volume number, and page rang, or URL link and its accessed month, date, and year for reference number 47.	
Q5	Please check reference numbers 27, 29, 30, and 53 for correctness.	
Q6	Please provide the volume number and page range or URL link for reference number 55.	

RESEARCH ARTICLE

Precipitation of cerianite crystals and its effect on the rheology of a simplified nuclear glass melt

J. Jiusti¹ | E. Regnier¹ | N. M. P. Machado¹ | M-L. Ghazzai¹ | V. Malivert¹ |
M. Neyret¹ | F Faure²

¹Laboratoire d'études de Développement des Matrices de Conditionnement, Centre de Marcoule, Univ Montpellier, Marcoule CEDEX, Bagnols-sur-Cèze, France

²Université de Lorraine, Nancy, France

Correspondence

J. Jiusti, CEA, DES, ISEC, DE2D, SEVT, Laboratoire d'études de Développement des Matrices de Conditionnement, Centre de Marcoule, Univ Montpellier, BP 17171, Bagnols-sur-Cèze, Marcoule CEDEX 30207, France.

Email: jeaninjiusti@gmail.com

Abstract

In France, high-activity level wastes resulting from nuclear fission are conditioned in a homogeneous sodium-aluminoborosilicate glass by high-temperature vitrification. The tolerance of even a small fraction of crystals could enable an increase in the waste loadings, in addition to promoting process flexibility. If the waste loading were to be increased in French nuclear glass, cerianite (CeO_2) crystals could precipitate. In this study, we investigated the cerianite crystallization in a simplified nuclear glass melt at different temperatures, Ce_2O_3 wt%, and shear conditions. Furthermore, the evolution of the viscosity along with cerianite precipitation was followed. It was found that Ce_2O_3 is highly soluble in the glass melt, as even for a Ce_2O_3 wt% as high as 10% wt, the cerianite fraction in dynamic conditions at 1100°C after 8 h of crystallization was less than 1% vol. In addition, shear strongly accelerates cerianite crystallization and a high Ce_2O_3 content can engender the precipitation of highly branched dendrites. The evolution of the cerianite fraction did not significantly affect the viscosity of the glass melt. Finally, unlike what has been observed in the well-known platinum group metal (PGM)-bearing melts, a glass melt containing .8 vol% of cerianite crystals remains Newtonian.

KEYWORDS

conditioning, crystallization, viscosity

1 | INTRODUCTION

In France, high-activity level wastes resulting from nuclear fission are conditioned in alumino-borosilicate glasses by high-temperature vitrification.¹ In this process, the calcined waste is mixed with the glass precursor and then heated to the vitrification temperature. For the hot crucible melter, the technology most commonly used in France, the temperature of vitrification is usually around 1100°C , but

in other furnace technologies it can be as low as 1000°C , as in the case of the in-can melter,^{2,3} and can reach up to 1250°C^{1-3} for the cold crucible technique. The waste-to-glass ratio is determined by considering the solubility of species coming from the calcine, in order to obtain a homogeneous melt. Exceeding solubility limits are generally avoided, because this can degrade the long-term behavior of the glass and also because the precipitation of particles can directly affect the physical properties of the

melt, changing or even compromising the technological feasibility of the vitrification process.^{4,5} The tolerance of even a small fraction of crystals during vitrification could lead to a more flexible process, allowing changes in the composition of the calcine or the immobilization of other types of nuclear wastes, in addition to increasing the waste loading.^{4,6}

Previous studies^{7–12} have shown that the presence of less than 1 vol% of platinum group metal particles (PGM: here, Ru, Rh, Pd) leads to a very shear thinning and thixotropic behavior. The high viscosities shown in PGM-bearing melts at low shear rate regimes are associated with its strong tendency for particle aggregation, which can significantly increase the effective particle volume fraction by trapping the liquid inside its aggregates. As well as affecting the rheological properties of the melt, PGM particles can engender changes in electrical conductivity and are prone to settling.^{8,13} Nonetheless, the extensive studies carried out in the last decade on the impact of PGM particles on the glass melt physical properties have contributed to a deeper understanding of this particle-melt system and consequently, to better control of the vitrification process.

Unlike PGM particles, crystals are soluble in the melt, and their fraction can fluctuate during the vitrification process.^{14–16} In the case of multicomponent melts, different crystals can precipitate,^{17,18} and the fraction of a particular crystal is a function of temperature and time.^{14, 19–22} In addition, the flow conditions can also affect crystallization. Different theoretical and simulation studies of hard sphere, colloidal, and simple liquid systems^{23–32} indicate that a gentle flow can increase both nucleation and crystal growth rate due to the increase in matter transport. In agreement with theoretical results, the rare experimental evidence available indicates that the crystallization kinetics of silicate melts are favored by stirring,^{33–35} but to our knowledge, no study on crystallization under dynamic conditions in nuclear glasses has been reported.

Among all the crystalline phases likely to precipitate in the French glassy matrix at higher waste loadings, cerianite (CeO_2) is the one stable at the highest temperatures, controlling the *liquidus* of the nuclear melt. For instance, cerianite has been reported to be stable up to 900°C for compositions containing as little as 1 wt% of Ce_2O_3 .^{17,18} Hence, an increase in the waste loading would potentially stabilize this phase at vitrification temperatures, and therefore the study of cerianite crystallization and its effect on melt properties is essential to properly control the process. Aside from being of interest in vitrification, cerianite presents a simple composition and cubic morphology, which is preferable for an initial study considering the numerous variables involved in crystallization.

In this work, we investigated cerianite crystallization in a simplified nuclear glass matrix at different temperatures,

Ce_2O_3 weight contents, and flow conditions (quiescent and dynamic) to define the cerianite composition-temperature domain, morphology, and effect of shear on crystallization. Furthermore, we studied the evolution of the viscosity along with cerianite precipitation, and compared the effect of cerianite particles on viscosity-shear dependency to that shown by PGM-bearing melts at an equivalent volume fraction.

2 | EXPERIMENTAL METHODS

For this study, a simplified nuclear glass series named CXX was used, where XX means the nominal Ce_2O_3 weight content. We elaborated the glasses and carried out crystallization and rheological studies, as shown in Figure 1 and detailed in the following sections.

2.1 | Glass elaboration and characterization

The glasses were synthesized from the following reagents: SiO_2 (Sibelco, 99.4%), Al_2O_3 (Sigma Aldrich, 98%), H_3BO_3 (VWR Prolabo, 100%), CaO (Sigma Aldrich, 99.9%), Nd_2O_3 (Sigma Aldrich, 99.9%), Na_2CO_3 (Acros Organicos, 99.95%), and CeO_2 (Sigma Aldrich, 99.9% and VWR Prolabo, 99.95%). The well-mixed reagents were melted in a platinum-rhodium (90%Pt-10%Rh) crucible (volume = 500 cm³) in a muffle furnace at the elaboration temperature (T_e , presented in Table 1) for 3 h. After this cycle, the melt was poured onto a stainless steel plate, and the glass obtained was ground. The resulting fine powder was replaced in the crucible and melted twice more. The total elaboration time at T_e was 7 h, and after the third plateau, the melt was quenched on a steel plate (at room temperature), and the glass disc obtained was annealed at 550°C for 6 h. Batches of about 200 g of glass were thus obtained.

An additional batch of 800 g of the C10 glass was elaborated in a furnace heated by the Joule effect. The well-mixed precursors were inserted into the furnace crucible at 1200°C slowly in order to control foaming due to reduction of Ce^{4+} to Ce^{3+} . The melt was then heated up to T_e , and remained at this temperature for 3 h before being quenched on a steel plate. A mechanical stirrer was used during the entire process to ensure melt homogeneity. This batch, named C10SG, was used for the experiments on crystallization in dynamic conditions.

A differential thermal analyzer (SETSYS Evolution, Setaram Instrumentation) with platinum crucibles was used to determine the glass transition temperature (T_g). The DTA curves are presented in the [Supplementary](#)

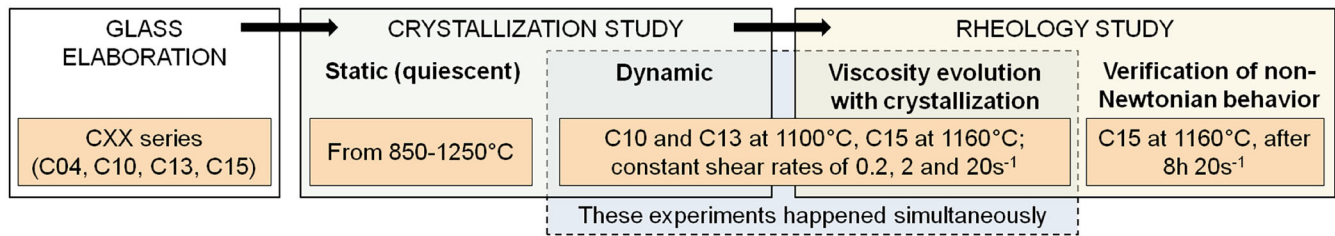


FIGURE 1 Flow chart showing the experimental methods used in this work.

TABLE 1 Nominal and measured compositions of the CXX glasses studied in this work in weight content. The nominal compositions are identified with an “N” together with the name of the glass. All glasses were elaborated in a muffle furnace, and one 800 g batch from C10 (C10SG batch) was elaborated in a furnace heated by the Joule effect. Composition was determined by electron probe microanalyzer (EPMA) (see text).

Oxide	C04 N	C04	C10 N	C10	C10SG	C13 N	C13	C15 N	C15
B ₂ O ₃	15.0	14.2	14.0	10.7	13.0	13.6	11.0	13.2	9.7
Na ₂ O	14.8	15.7	13.9	13.6	15.8	13.4	12.5	13.1	12.1
Al ₂ O ₃	5.3	5.6	5.0	4.5	5.1	4.8	5.2	4.7	5.2
SiO ₂	49.3	49.0	46.2	49.7	45.1	44.7	46.8	43.7	46.4
CaO	5.8	5.4	5.4	5.0	5.4	5.2	5.4	5.1	5.4
Ce ₂ O ₃	4.0	4.2	10.0	11.0	10.1	13.0	13.4	15.0	15.8
Nd ₂ O ₃	5.9	5.9	5.5	5.5	5.4	5.3	5.7	5.2	5.5
Sum	100.0	100.0	100.0	100.0	100.0	100.0	100.0	100.0	100.0
T _e		1250°C		1350°C	1350°C		1380°C		1400°C

Section. The mass density ρ of the glasses was measured at room temperature by the Archimedes principle, using a high precision balance (AT200, Mettler Toledo). Glass homogeneity and the absence of inclusions were verified by scanning electron microscopy (SEM) analyses (Supra 55 FEG, Zeiss). The viscosity at high temperature was determined using the rheometer-furnace-rotor setup described in Section 2.3.

A Cameca SX Five FE TACTIS electron probe microanalyzer was used to perform elemental analysis of the glasses obtained. Quantifications were carried out at 12 kV, 10 nA with a 10 μ m beam spot on the glass matrix. A TAP crystal was used to detect the $K\alpha$ of Na, Si, and Al, a LiF crystal to detect the $L\alpha$ of Nd, a PET crystal to detect the $K\alpha$ and $L\alpha$ of Ca and Ce, and a PC3 crystal to detect the $K\alpha$ of B. The compositions measured are presented in Table 1.

2.2 | Crystallization in static (quiescent) conditions

Isothermal treatments from 850 to 1250°C were carried out in a tubular furnace with an 80 \times 30 \times 20 mm chamber that ensures a maximal temperature variation of $\pm 2^\circ$ C. The

glasses were treated in closed platinum capsules to avoid the volatility of Na and B. The heat treatments lasted 24 h each, as it was considered that this duration was enough to reveal the thermodynamically stable crystals in each glass-temperature condition. An additional heat treatment mimicking the thermal cycle used in the dynamic experiments (plateau of 10 min at 1350°C + plateau of 8 h at 1100°C + cooling in air) was performed with the C10SG glass to allow comparison between the quiescent and dynamic conditions. Since the interest was to determine the stable crystals, finely powdered glass was used in order to accelerate crystallization by heterogeneous nucleation. The treated sample was retrieved by cutting the tips of the capsules and collecting the glass pieces. These pieces were then embedded in epoxy resin and polished prior to analysis by SEM (Supra 55 FEG, Zeiss), in order to determine which crystals (if any) were present.

2.3 | Crystallization in dynamic conditions

The dynamic experiments were carried out using the rheometer-furnace-rotor setup shown in Figure 2A. The equipment consisted of a stress-imposed rheometer

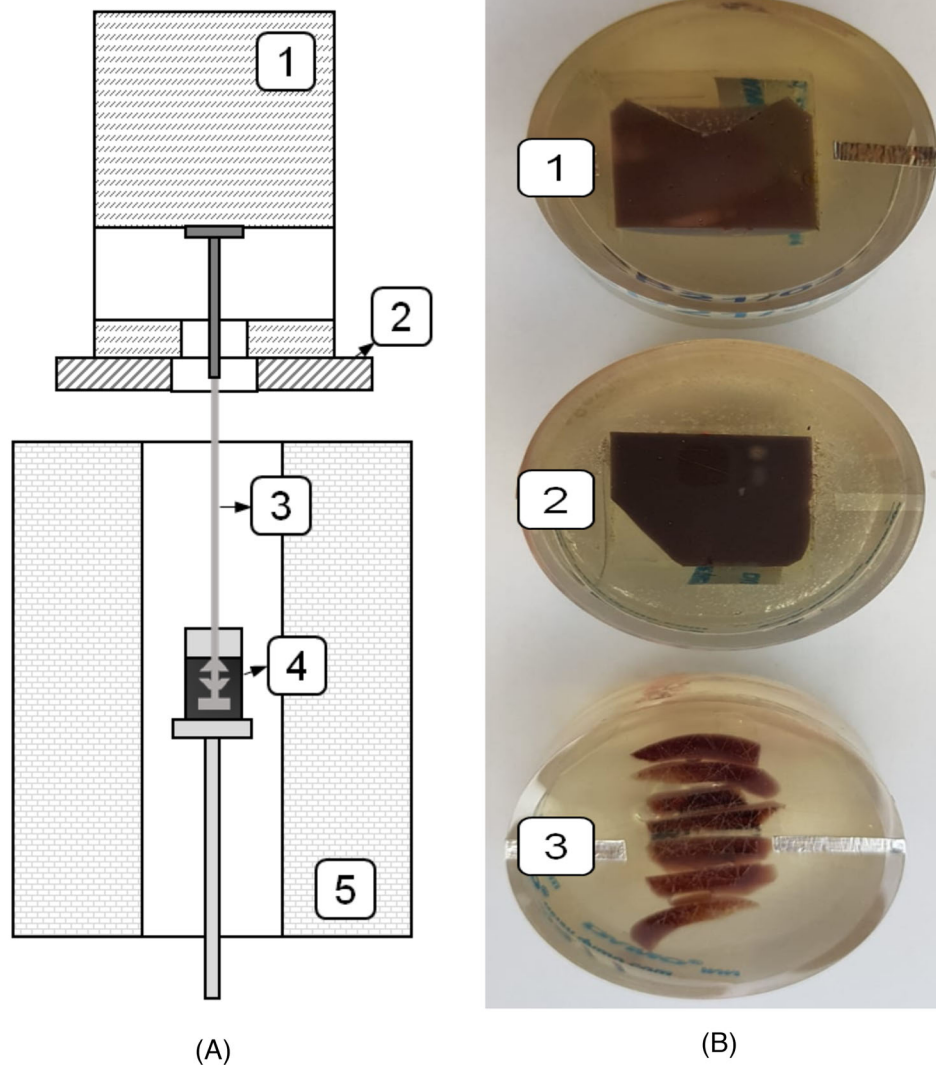


FIGURE 2 (A) Rheometer-furnace setup for viscosity measurements: 1-Rheometer, 2-Rheometer support, 3-Multiblade rotor, 4-Standard platinum crucible for viscosity measurements, and 5-Furnace. (B) Photos of the polished sections obtained for each condition of crystallization in dynamic conditions: 1-top and 2-bottom of the crucible, 3 - Multiple pieces that were in contact with the crucible.

(Rheometrics Scientific SR5000)¹ fixed on a support² where a rotor³ was attached. This rotor was immersed in molten glass contained in a platinum-rhodium crucible (13.5 mm radius and 40 mm length)⁴ placed at the center of a vertical tubular furnace⁵ ($T_{\max} = 1500^{\circ}\text{C}$). The geometry used was a multi-blade rotor with a 9-mm radius and 27-mm long, detailed in Puig et al.⁹ The pair composed of the crucible and the multi-blade geometry formed a virtual Couette cell, for which an analogy with the concentric cylinder geometry is necessary (i.e., Couette analogy) to extract the viscosity/shear-rate curves from the data.³⁶ The rheological parameters (shear stress σ , strain γ , shear rate $\dot{\gamma}$) were obtained from the geometrical factors determined via the calibration procedure described in Puig et al.⁹

In order to observe the crystallization behavior in conditions similar to those encountered in the vitrification

TABLE 2 Conditions of the dynamic crystallization experiments.

Glass	Condition	Temperature ($^{\circ}\text{C}$)	Shear rate (s^{-1})	Time (h)
C10SG	1	1100	0.2	8
C10SG	2	1100	2	8
C10SG	3	1100	20	2
C10SG	4	1100	20	4
C10SG	5	1100	20	8
C13	6	1100	20	8
C15	7	1160	20	8

furnace, seven different conditions were created (Table 2) by submitting the samples to three different shear rates

corresponding to three shear regimes: high, medium, and low shear (20, 2, and $.2 \text{ s}^{-1}$, respectively).

For each experiment, the filled crucible was inserted into the furnace and heated up to the elaboration temperature (see Table 1) to dissolve crystals that might have formed during the filling step. The temperature was maintained for 10 min, and then decreased by $\sim 30^\circ\text{C}/\text{min}$ (controlled by the inertia of the system) to the chosen measurement temperature (1100 or 1160°C). After the crystallization experiments according to the conditions shown in Table, the crucible was removed from the furnace with a controlled descent speed of about $2 \text{ cm}\cdot\text{min}^{-1}$ to avoid further crystallization while preserving the furnace components. With this method, the approximate cooling rate was $30^\circ\text{C}/\text{min}$. The samples were then annealed at 550°C for 6 h in order to remove the residual stresses in the glass.

The annealed samples were removed from the crucible by drilling, giving cylinders 20 mm in diameter and approximately 25 mm in height. Small pieces of glass that were located between the crucible wall and the drilling tool while the core was being removed were also recovered. The cylinders obtained were cut in half along the longitudinal axis, and one of each resulting semi-cylinders was cut in half along the transversal axis. The two samples thus obtained were embedded in resin and their surfaces were polished before SEM analysis. The glass pieces were also embedded so that the surface formerly in contact with the crucible wall could be analyzed. Three polished sections were obtained for each condition: (1) the top and (2) the bottom half of the crucible, and (3) pieces of the “border” region of the crucible (Figure 2B).

2.4 | Postmortem analysis (after crystallization under dynamic conditions)

The cerianite fraction of the polished Sections 1 and 2 (Figure 2B) for each crystallization condition was determined by both image and chemical analyses. SEM images were acquired and processed using the protocol described in ref. [18] and [11]. The entire surface (approximately 200 mm^2) of each polished section was mapped with a 250x magnification. The crystallized area fraction was obtained from image processing using the ImageJ free software. As the distribution of the cubic crystals was homogeneous within the sample, we considered that the area fraction is equivalent to the volume fraction ($\Phi_{\text{surf}} = \Phi_{\text{vol}}$).³⁷ We also collected the Feret diameter (the longest distance between two parallel planes restricting the object perpendicular to that direction) and the density per area of cerianite crystals from the ImageJ analysis report.

The composition of the glass matrix and crystals after crystallization was determined by EMPA, as described

TABLE 3 Properties of the CXX glass series. The digits in brackets are the uncertainty of the least significant number.

Ident.	%Ce ₂ O ₃	Density (g/cm ³)	T _g (°C)	T _L (°C)
C4	4.2(1)	2.677(3)	566(3)	987 < T _L < 1011
C10SG	10.2(1)	2.792(1)	571(3)	–
C10	11.0(1)	2.806(2)	566(3)	1159 < T _L < 1184
C13	13.6(1)	2.867(1)	576(3)	1184 < T _L < 1207
C15	15.8(1)	2.911(2)	577(3)	1232 < T _L < 1254

in Section 2.1. To ensure that the crystal was not taken into account by the electrons’ interaction volume, the measurements were made a few micrometers from the crystals. About 50 points were measured in order to obtain good accuracy and verify any possible heterogeneity in the glass matrix. Because of the evaporation of B₂O₃ and Na₂O during the dynamic experiments, the Ce₂O₃ variation in the glass matrix composition was determined by the Ce₂O₃/SiO₂ ratio, since SiO₂ is less susceptible to evaporation. The CeO₂ crystal fraction was then determined by Equations 1 and 2, where the cerianite density ($\rho_{\text{cerianite}}$) is equal to $7.28 \text{ g}\cdot\text{cm}^{-3}$.³⁸

$$\begin{aligned} \%Ce_2O_3 \text{ consumed} &= \%Ce_2O_3 \text{ parent glass} \\ &- \left(\frac{\%Ce_2O_3}{\%SiO_2} \%SiO_2 \text{ parent glass} \right) \end{aligned} \quad (1)$$

$$\%Cerianite \cong \frac{\rho_{\text{glass}}}{\rho_{\text{cerianite}}} \%Ce_2O_3 \text{ consumed} \quad (2)$$

Polished sections containing the glass pieces previously in contact with the crucible wall (item 3 in Figure 2B) were also analyzed by SEM, applying the same protocol as that used for the other polished sections.

The sample obtained from condition 5 (Table 3) was analyzed by synchrotron X-ray microtomography in order to recreate the 3D shape of the cerianite crystals and their spatial distribution. The microtomograph of the European Synchrotron Radiation Facility (ESRF, ID19 beamline, Grenoble, France) was used to scan pieces a few millimeters thick taken from the bulk and border regions (i.e., one sample from the recovered cylinder and one from the shattered glass). A volume of approximately 1 mm^3 with a resolution of $1.6 \mu\text{m}$ was mapped.

In addition to chemical analyses by EMPA, Raman and XRD analyses were performed after crystallization to confirm the nature of the cerianite crystals. For the XRD analyses, two different samples were involved: (1) Fragments that had been in contact with the platinum crucible wall of an additional sample of C10 glass heat treated in

static conditions in a muffle furnace for 24 h at 1100°C (after an additional treatment, because the sample coming from the platinum capsule was too small), and (2) a fragment of the sample recovered from the C10SG 20 s⁻¹ 8 h condition, whose glass matrix was partially dissolved in nitric acid in order to improve the concentration of the crystals. Both samples were ground, and the analyses were performed with an X'Pert PRO PANalytical instrument using Cu-K α radiation ($\lambda = .15406$ nm). XRD patterns were collected in standard ($\theta-2\theta$) geometry between 20 and 80° and a step of .013°. The Raman analyses were performed on several crystals in the bulk of the samples C10SG .2 s⁻¹ 8 h, C10SG 20 s⁻¹ 8 h, C13 20 s⁻¹ 8 h, C15 20 s⁻¹ 8 h, the sample of C10SG previously heat treated in a platinum capsule mimicking the thermal cycle used in the dynamic experiments, and crystals of surface of the condition C10SG 20 s⁻¹ 8 h, that is, six samples in total. A Raman Horiba Jobin-Yvon HR800 spectrometer equipped with an argon laser as excitation source (532 nm) was used.

2.5 | Rheological behavior

A rheology study was carried out simultaneously with the dynamic crystallization experiments described in 2.3, that is, the viscosity data were acquired while the crystallization occurred. In addition, a steady state regime measurement was performed with the C15 glass after crystallization (condition 7 in Table 2 was repeated) to investigate the existence of non-Newtonian behavior. The measurement consisted in imposing successive shear stress values from 200 Pa to 0.8 Pa (after a pre-shear of 200 Pa for 60 s). This test was done to compare the rheological behavior of this system with previous results obtained for a PGM-bearing melt.^{9,10}

3 | RESULTS

3.1 | Glass characterization and crystal domains

The measurement results for Ce₂O₃ wt%, density, glass transition, and *liquidus* temperature of each glass are shown in Table 4. The density of the glass rose as the Ce₂O₃ was increased, due to the high molar mass of Cerium. A linear regression between Cerium content and glass density resulted in the equation $\rho(\pm 0.02 \text{ g.cm}^{-3}) = 0.021[\% \text{wtCe}_2\text{O}_3] + 2.58$ ($r^2 = 0.993$). The glass transition temperatures for C4, C10, C10SG, C13, and C15 determined based on thermal analysis were 566, 571, 566, 576, and $577 \pm 3^\circ\text{C}$, respectively. Although it is generally accepted that cerium plays a role of network modifier, some studies reported that it can play a dual

role in a glass structure (glass network modifier or a glass network former) depending on its content.^{39,40} The slight T_g increase observed when Ce₂O₃ increased can be an indication that for the Ce₂O₃ content range studied here, cerium can act as a glass network former, or, as proposed by Wang et al.⁴⁰ it can enhance linkage and compactness of the glass structure.

In the interval of T_L shown in Table 4, the minimum value is the highest temperature for which cerianite crystals were observed after the 24 h heat treatment, and the maximal value is the lowest temperature for which no crystals were observed after 24 h. For the composition range studied, the liquidus temperature can be approximated by $T_L (\pm 25^\circ\text{C}) = -0.73[\% \text{wtCe}_2\text{O}_3]^2 + 35[\% \text{wtCe}_2\text{O}_3] + 866$ ($r^2 = 0.97$).

Figure 3 shows the SEM micrographs of the glasses C10, C13, and C15 treated at different temperatures for 24 h. The presence of cerianite (cubic crystals) and apatite (acicular crystals) can easily be identified in the images, as already extensively discussed in previous studies of similar aluminoborosilicate nuclear glasses.^{18,41,42} In Figure 4, the cerianite-only domain is found in terms of temperature and Ce₂O₃ wt% content.

For both apatite and cerianite domains, the maximum temperature increased with the cerium content. The cerianite is stable above 1000°C (the in-can melter vitrification temperature) from about 4 wt% of Ce₂O₃. The results indicate that Ce₂O₃ has a high solubility in the glass matrix at the temperatures explored here (in agreement with what has been found in previous studies⁴³) and that the cerianite crystallization kinetics are very slow for all the conditions of shear and Ce₂O₃ wt% studied. Figure 4 indicates that an increase in the lanthanide content able to be incorporated into the apatite structure can stabilize it at higher temperatures, and possibly at the temperature range of the vitrification process. For the glass system studied in this work, apatite is expected to be stable above 1000°C from about 8 wt% Ce₂O₃.

Based on the interest of this work the composition C10 was chosen to initiate the study in dynamic conditions, since it showed the cerianite temperature domain between 1060 and 1159°C, which is centered within the vitrification temperature of the hot crucible melter ($\sim 1100^\circ\text{C}$).

3.2 | Crystallization in dynamic conditions

As described in Section 2.3, nine different crystallization experiments were carried out in dynamic conditions. The cerianite fractions determined by chemical and image analyses for each of these conditions are presented in Table 4.

TABLE 4 Cerianite fraction, mean Feret diameter, characteristic crystal size (S), and crystal volumetric density for the different dynamic crystallization conditions. The digits in brackets are the uncertainty of the least significant number.

Glass	Cond.	Temp. (°C)	Shear rate (s ⁻¹)	Time (h)	Cerianite fraction (vol%)		Mean Feret diameter (μm)	S (μm)	Crystal volumetric density, N _V (10 ² m ⁻³)
					Image analysis	Chemical analysis			
C10SG 1	1	1100	0.2	8	0.011(2)	0.22(1)	3.5(2)	4.8	9(1)
C10SG 2	2	1100	2	8	0.11(2)	0.36(2)	9.0(5)	13.0	5.0(6)
C10SG 3	3	1100	20	2	0.006(1)	0.11(1)	3.6(2)	3.7	11(1)
C10SG 4	4	1100	20	4	0.09(2)	0.36(2)	12(1)	13.2	4.0(5)
C10SG 5	5	1100	20	8	0.18(3)	0.65(3)	25(1)	21.5	1.8(3)
C13	8	1100	20	8	0.56(5)	0.87(4)	–	–	–
C15	9	1160	20	8	0.82(6)	1.2(1)	–	–	–

Figure 5 shows the cerianite volume fraction (Φ) determined by image and chemical analyses for the different conditions studied. Considering the results of the chemical analyses for the shear rate of 20 s⁻¹ (Figure 5A), the cerianite content increased with time, reaching 0.65 vol% after 8 h of crystallization. For the same experiment duration, the conditions of crystallization at 0.2 and 2 s⁻¹ (Figure 5B) resulted in a cerianite volume content of 0.22% and 0.36%, respectively, which means the overall crystallization kinetics seem to be accelerated by shear. The highest cerianite fraction (1.2 vol%) was obtained for the C15 glass after 8 h of crystallization under the highest shear rate (20 s⁻¹) (Figure 5C).

The fraction determined by image analysis is always lower than that determined by chemical analysis, but roughly the same trend can be observed for both results. The difference between the data is probably due to cerianite's strong tendency to heterogeneous crystallization, which occurs on the crucible wall and rotor blades, and this is not accounted for in the quantification by image analysis. In this consideration, the image quantification would give the crystal fraction in suspension in the melt (bulk), and the chemical analysis would give the total amount of cerianite (bulk + surface). In fact, an effect on both bulk and surface crystallization was noticed in the samples, and the results and discussion regarding crystal morphology and size are presented separately in the following sections.

3.2.1 | Bulk crystallization

In Figure 6, we present mosaics of SEM images of the bulk samples for each crystallization condition. The bigger images (images for the crystallization conditions of 20 s⁻¹ and 8 h) represent an area of about 12 mm² each, and the smaller ones are about 6 mm² each. On the left of Figure 6, images of all the crystallization experiment conditions per-

formed with the C10SG glass are presented. From these images, it can be seen that as the time of experiment and shear increased, the cerianite fraction rose, as already shown in the crystal fraction values in Table 4 and Figure 5. Additionally, an evolution of crystal size with both applied shear and time can be observed. On the right of Figure 6, the different Ce₂O₃ wt% is compared, and as well as the obvious increase in crystal fraction, an evolution of crystal morphology is also noticeable.

From the image analyses, the number and size of crystals could also be determined. The volumetric number density of crystals (N_V) can be calculated from the number of crystals per unit of area determined from image analyses (N_A) and the characteristic crystal size (S) as in Equation (3).^{44,45}

$$N_V = \frac{N_A}{S}. \quad (3)$$

The characteristic crystal size S is determined by:

$$S = \left(\frac{\phi}{N_A} \right)^{0.5}, \quad (4)$$

where Φ is the area fraction determined by image analyses (from Table 4). The calculated values of S, N_V are shown in Table 4. The determination of crystal size based on the image analyses can be subject to errors due to the 2D limitation, and therefore it does not precisely represent the real size distribution. Nevertheless, analyses of crystal size give essential insights into the effect of shear rate on crystal growth. In this work, the Feret diameter was used to compare the conditions studied, and more than 2000 particles were analyzed for each condition. The evolution of the number of crystals per volume unit (N_V) and Feret diameter are shown in figure 7A,B. The cumulative distributions of the crystal Feret diameters are plotted in Figure 8. The crystal density and size distribution were not

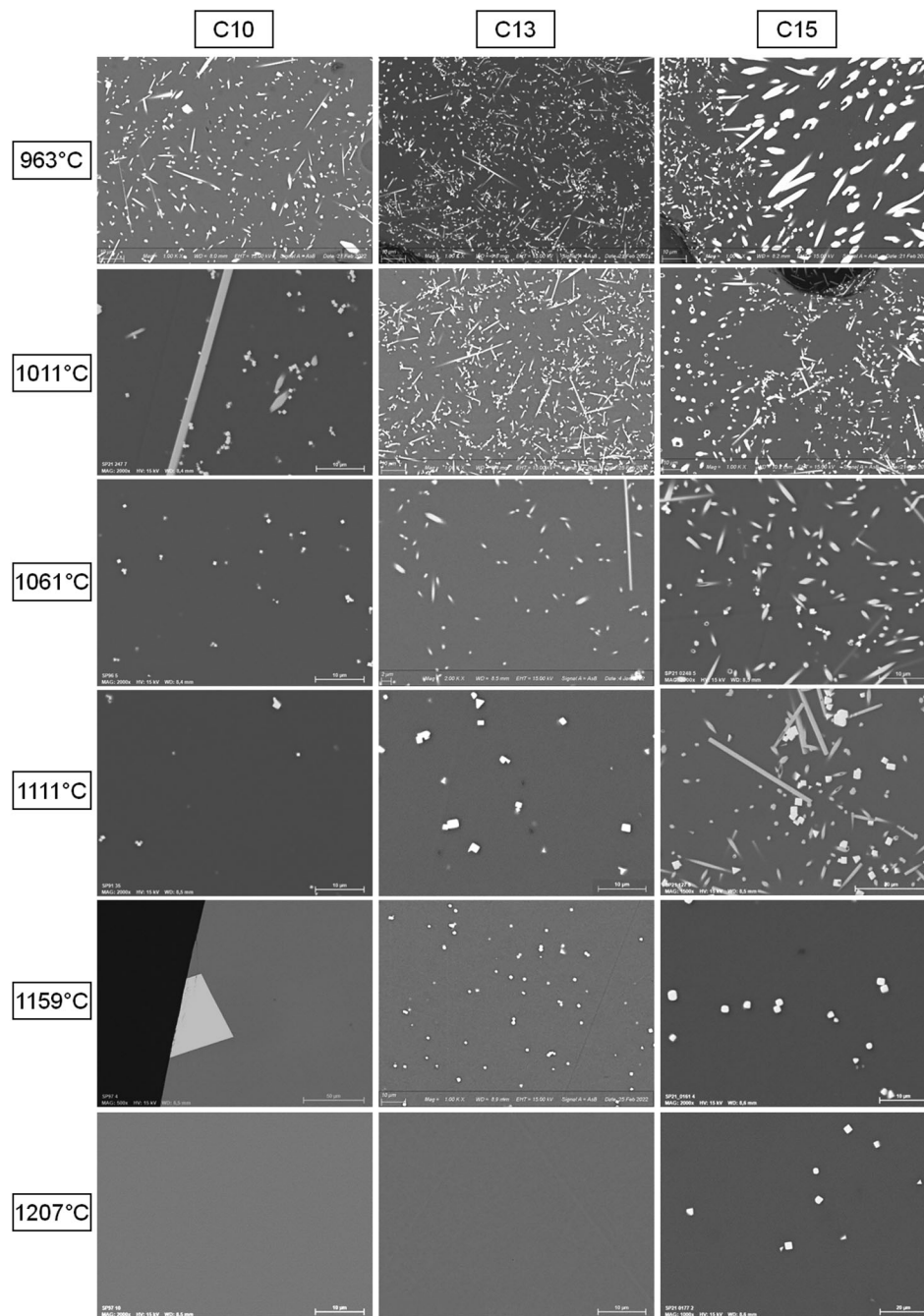


FIGURE 3 Scanning electron microscopy (SEM) images of the heat treated samples in static conditions. The compositions and temperatures are indicated in the top and left side of the figures. The images were obtained at a magnification of 500 to 2000X.

determined for the C13 and C15 glasses because the complex morphology of the crystals significantly degraded the image analysis.

In Figure 7A, the calculated number of crystals per unit of volume (N_V) at 2 h was about 10^3 mm^{-3} , and this decreased to about 10^2 mm^{-3} at 8 h as crystallization developed. Likewise, the N_V decreased as the imposed shear was increased (Figure 6B). The calculated N_V at 2 h of crystallization at 20 s^{-1} was similar to that observed after 8 h of

crystallization at 0.2 s^{-1} . In both cases, the decline of nucleated crystals was followed by an augmentation of the mean Feret diameter: the mean Feret diameter was 3.6, 12, and $25 \mu\text{m}$ for the conditions of 2, 4, and 8 h, respectively, and 3.3, 9.0, and $25 \mu\text{m}$ after 8 h of crystallization at the shear rates of 0.2, 2, and 20 s^{-1} , respectively.

Figure 8A shows a coherent evolution of the crystal size distribution with the duration of the experiment. After 2 h, most crystals (about 88%) had a Feret diameter below

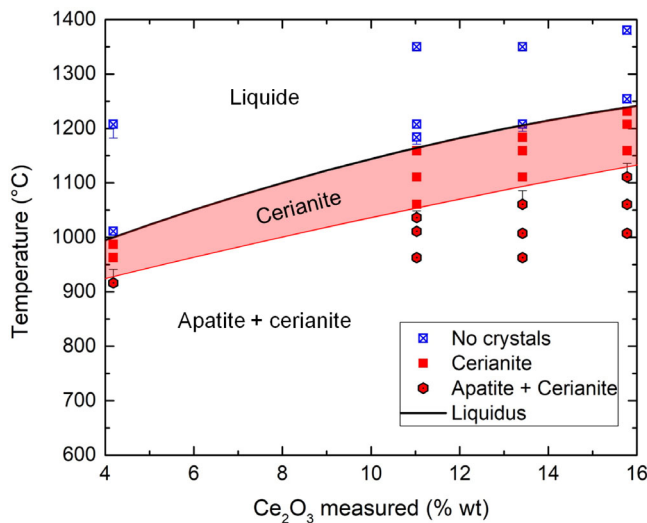


FIGURE 4 Cerianite and apatite domain as a function of Ce_2O_3 %wt content and temperature. \square : no stable crystalline phase, \blacksquare : cerianite is the only stable phase, hexagons: apatite + cerianite.

5 μm , while for 4 and 8 h, the quantities of crystals with a
6 Feret diameter of less than 5 μm were 71 and 40%, respec-
7 tively. When comparing the different conditions of shear in
8 Figure 8B, the same overall behavior as that described with
9 time can be observed. For the condition at 0.2 s^{-1} , 96% of
10 the crystals had a Feret diameter below 5 μm , and a few
11 well-developed crystals reaching 100 μm also appeared. It
12 is possible that these big crystals may have originated dur-
13 ing the crucible filling and resisted the dissolution step
14 during the beginning of the experiment, hence had more
15 time to grow. For the crystallization at 2 s^{-1} , 88% of the
16 crystals had a Feret diameter of less than 5 μm , and for the
17 20 s^{-1} condition, only 40%.

18 In Figure 9, we present several images of crystals
19 arranged schematically to allow a better comparison of
20 their morphology. The top line of the figure shows the
21 three conditions of time (2, 4, and 8 h), and the center line
22 shows the three conditions of shear (0.2 , 2 , and 20 s^{-1}),
23 both for the C10SG glass at 1100°C . The bottom line shows
24 the three different compositions (C10SG, C13, C15) after 8 h
25 of crystallization at 20 s^{-1} . The figure of condition C10SG -
26 20 s^{-1} - 8 h appears three times. For the shortest experi-
27 ment duration at 20 s^{-1} , there are mainly small particles (of
28 about 3 μm) and some star-shaped particles with Feret
29 diameters greater than $\sim 50 \mu\text{m}$ which have eight branches
30 (considering 3D), characteristic of dendritic morphology.
31 The crystals grew as the experiment duration increased,
32 and became concave cubes after 8 h. A 3D view of the crys-
33 tals for the condition C10SG 8 h 20 s^{-1} (Figure 10A) shows
34 multiple hollow cubic crystals randomly distributed in the
35 glass, which means that the different shapes observed in

the 2D images (Figure 9) are distinct planes of concave
cubes (Figure 10C). Less frequently, some crystals showing
an octapod morphology (Figure 10B), that is, a cube with
eight other small cubes developed in the corners, are visi-
ble. This morphology suggests that, as well as the increase
in crystal size, longer experiment duration leads to crystal
overgrowth.

Regarding the different conditions of shear, for the
 0.2 s^{-1} condition we see mainly small round particles with
diameters of about 3 μm and a few developed crystals
whose dendritic nature is obvious. The crystals obtained
for the 2 s^{-1} condition seem to be dendritic crystals that
have ripened like those observed for the 20 s^{-1} . The
increase in Ce_2O_3 wt% seems to have the greatest effect on
the cerianite morphology. Some highly branched dendritic
crystals developed for both the C13 and C15 glasses, as can
be seen in Figure 9 and also in Figure 6, where a dendritic
branch of about 500 μm is visible in the SEM images of the
C15 sample.

3.2.2 | Surface crystallization

Figure 11 shows representative regions of the recovered
glass pieces that were in contact with the crucible wall dur-
ing the dynamic experiments. The linear nuclei density and
biggest crystal size could be determined by analyzing the
crystallized layer from the conditions of the C10SG
glass. A length of at least 50 mm was analyzed for each
condition, in order to obtain reliable data. The nucleus
counting was done manually and considered only the
crystals previously in contact with the crucible surface.
The results are shown in Figure 7C,D, where the biggest
crystal size presented is an average of the size of the 10
biggest crystals measured. The determination of the nuclei
density for the C13 and C15 glasses was subject to a con-
siderable error due to the complexity of the crystal layers
formed, and therefore it was not determined for these
glasses.

As observed for bulk crystallization, the cerianite
surface crystallization was affected by the duration of the
experiment, applied shear rate, and glass composition.
Both Figures 11 and 7C show an evolution in the size of
the biggest crystals with time, where crystals reach up to
370 μm after 8 h of crystallization at 20 s^{-1} . When com-
paring the number of nuclei per mm, we see an increase
from 2 to 4 h, and then a decrease for the condition of 8 h.
The crystal morphologies are dendritic in all samples, as
observed for the crystals in the bulk, and show a ripened
morphology at 8 h, as the branches of the dendrites take
on a more cubic shape after 8 h (more obvious in the
3D images shown in Figure 10D). When comparing the
samples for the different conditions of shear, an evolution

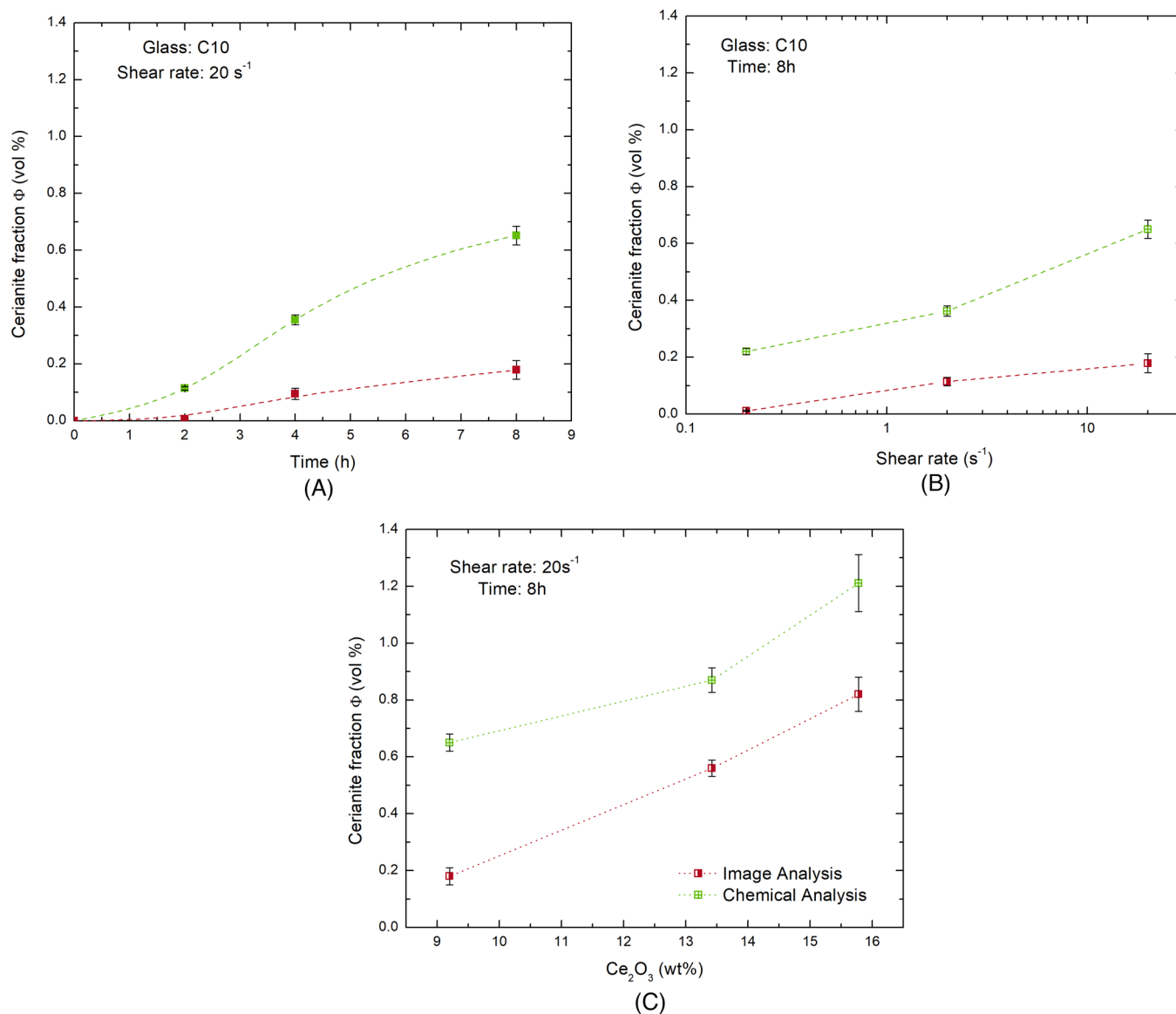


FIGURE 5 Evolution of the cerianite fraction as a function of (A) time, (B) applied shear rate, and (C) measured Ce₂O₃ wt%. Red squares: fraction determined by image analyses, and green squares: cerianite fraction determined by chemical analyses. The lines are drawn to guide the eye.

in crystal size is even more evident. At a shear rate of 0.2 s⁻¹, a layer of only about 20 μm was formed, while crystals reaching up to 370 μm can be found in the sample submitted to a shear rate of 20 s⁻¹ (as previously commented). At the same time, the number of nuclei per mm decreased as the shear rate increased. The Ce₂O₃ content showed the most pronounced effect on the crystal layer. The size of crystals reached up to 650 μm and 1 mm for C13 and C15, respectively. For the C15 composition, the higher temperature of the experiment might also play a role in crystal growth, as the diffusion rate increases with temperature.

3.3 | Cerianite characterization

The XRD of both samples prepared as described in Section 2.4 are shown in Figure 12A. In both of them, cerianite crystals (CeO₂) could be identified (JCPDS 43-1002). The Raman spectra (normalized to the greatest absolute intensity) of the different samples are shown in Figure 12B; the spectrum of cerianite crystal was added to the plot for comparison. The intense band located at 466 cm⁻¹ that corresponds to the F_{2g} phonon symmetry of cerianite is present in all spectra, as well as the weak band at 1180 cm⁻¹.⁴⁶ The weak bands observed at 270 and 315 cm⁻¹

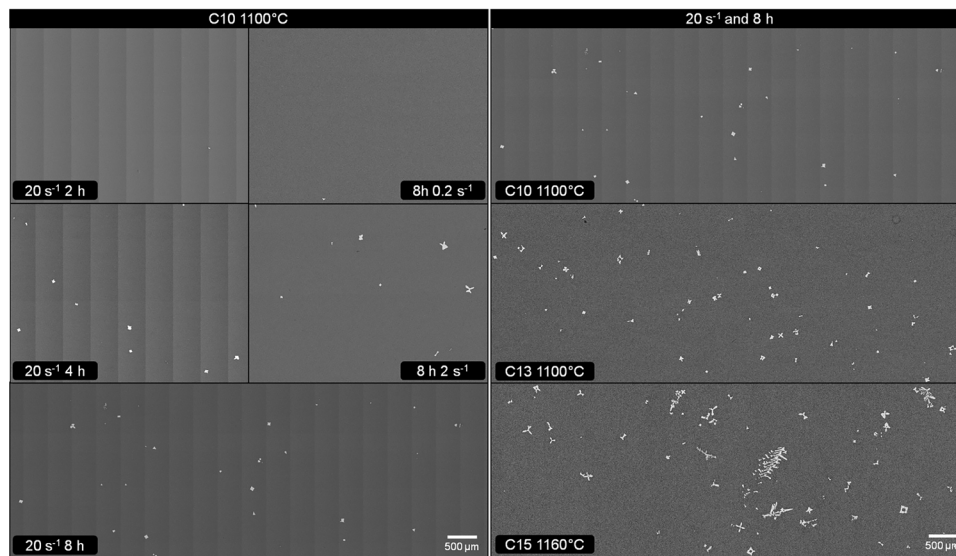


FIGURE 6 Scanning electron microscopy (SEM) images of the samples recovered for each condition of crystallization carried out in the rheometer. The left images show all five conditions for the C10SG glass, and the right images compare C10SG, C13, and C15 for the same conditions of shear and duration. All the experiments were performed at 1100°C, except for C15 glass.

were previously attributed to surface modes. The small bands at 550 cm^{-1} that appeared in all samples are reportedly linked to oxygen vacancies, but neither a red shift in the F_{2g} band nor a band at 2300 cm^{-1} corresponding to the presence of Ce^{3+} in the crystals were observed. Therefore, the oxygen vacancies could be due to a few substitutions for Ce^{4+} by Nd^{3+} (present in the glass compositions), although a high intensity peak is expected when a major substitution occurs and no evidence of Nd substitution was found in the XRD analyses.⁴⁶ More importantly, no difference regarding composition (C10, C13, C15) or shear condition (static, 0.2 or 20 s^{-1}) was observed.

3.4 | Rheological behavior

3.4.1 | Viscosity evolution during crystallization

The viscosity data acquired simultaneously with the crystallization experiments in dynamic conditions are presented in Figure 13, represented as relative viscosity η_R , which is the apparent viscosity during crystallization divided by the viscosity of the liquid η_L . The experiments performed with the C10SG glass are shown in Figure 13A, and the comparison between the different compositions for the condition at 20 s^{-1} for 8 h is shown in Figure 13B.

Figure 13A shows no significant change in the viscosity of the C10SG glasses for any of the conditions. The viscosity increment after 8 h was nearly the same ($\sim 15\%$) for the experiments at 2 and 20 s^{-1} , even though the cerianite frac-

tion was different (0.20 and 0.75%, respectively). For the 0.2 s^{-1} condition, the oscillation of the rotor makes it difficult to estimate the viscosity increment properly, but based on the average value the increase would be $\sim 7\%$. Figure 13A also shows that for the C10SG glass, the relative viscosity curves for the three conditions at 20 s^{-1} overlap, indicating good reproducibility of the experiment.

3.4.2 | Postcrystallization behavior

According to the results from Section 3.2.1, condition 9 resulted in a $\Phi = 0.82 \pm 0.06\%$ (or $\Phi = 1.2 \pm 0.1\%$ by chemical analysis), which is comparable to the PGM fractions studied in.^{9–11} We therefore repeated the crystallization experiment for condition 9 and then evaluated the effect on viscosity as a function of the shear stress (τ). Figure 14 shows the results from the C15 glass together with the results of previous studies for similar conditions of temperature and particle fractions.

The rheograms of all PGM-bearing melts shown in Figure 14 exhibit a Newtonian plateau at low shear, followed by a drop in viscosity and a second Newtonian plateau at high shear. The increase in viscosity from high to low shear occurs from a critical stress (τ_c), and the whole rheogram can be described by a simplified Cross model extensively discussed elsewhere.^{10,11,47} For a volumetric content of 0.7%, Puig et al.¹¹ verified a viscosity at a low shear rate that was 300 times higher than the viscosity at high shear. On the other hand, this work showed that a system containing 0.8 vol% of cerianite

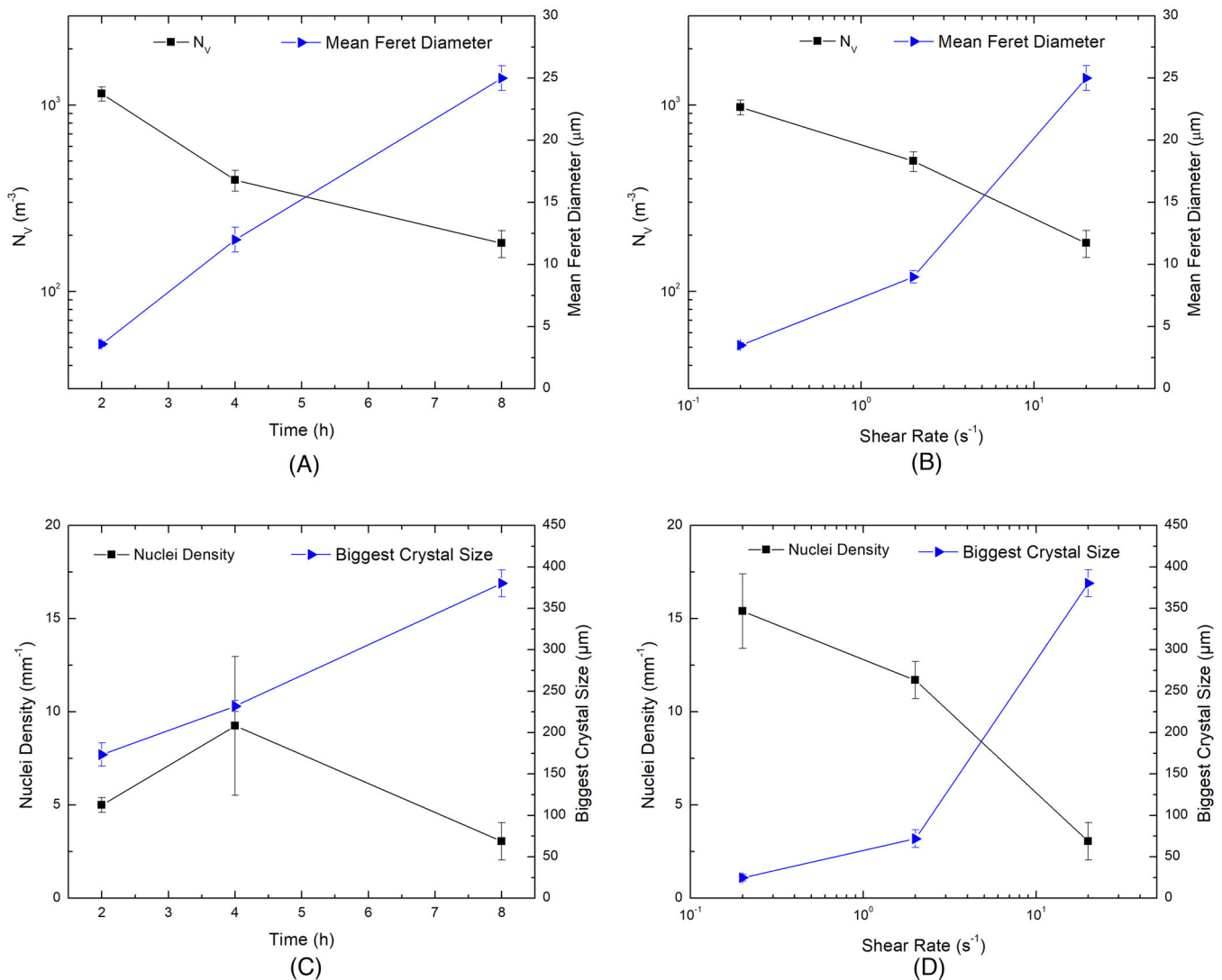


FIGURE 7 Evolution of volumetric nuclei density and mean Feret diameter with (A) time and (B) shear rate, and evolution of linear nuclei density and biggest crystal size with time (C) and shear rate (D). C10SG glass at 1100°C. The lines are included to guide the eye.

crystals continued to show Newtonian behavior, like the glass with no suspended particles studied in.¹¹

4 | DISCUSSION

4.1 | Crystallization in dynamic conditions

The system studied here can be considered as a solution within which cerianite (CeO_2) crystals precipitate at sub-liquidus temperatures. In this case, the cerianite fraction is expected to increase up to an equilibrium fraction that depends on the cerium concentration and the temperature at which the crystallization is taking place. Cerianite nucleates on surfaces (such as the crucible wall) and in the bulk (homogeneous nucleation), and the nucleated

crystals grow to reach the equilibrium fraction. Both nucleation (on the surface and in the bulk) and crystal growth happen concomitantly, and their rates depend on the thermodynamic and kinetic parameters of the system.^{14, 48–50} In addition, the morphology of a crystal evolves from a euhedral to a dendritic morphology by increasing the driving force towards crystallization, that is, the degree of supersaturation.^{50–54}

The overall behavior for both bulk and surface crystallization involved an increase in the cerianite fraction (Φ) with time and shear rate, accompanied by a decline in the number of nuclei (N_v) and an augmentation of crystal size. The decrease in the number of nuclei shown in Figure 7A as the crystallization developed can be explained by the Ostwald ripening phenomenon. As a system advances towards equilibrium, the small crystals dissolve, and the larger crystals continue to grow because larger crystals

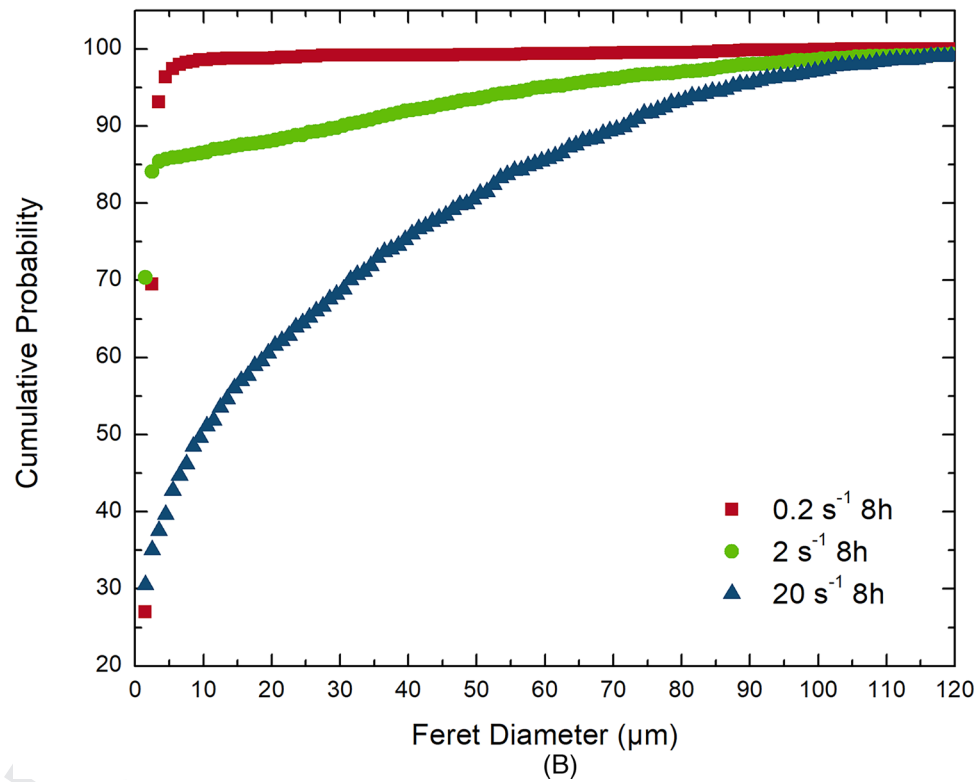
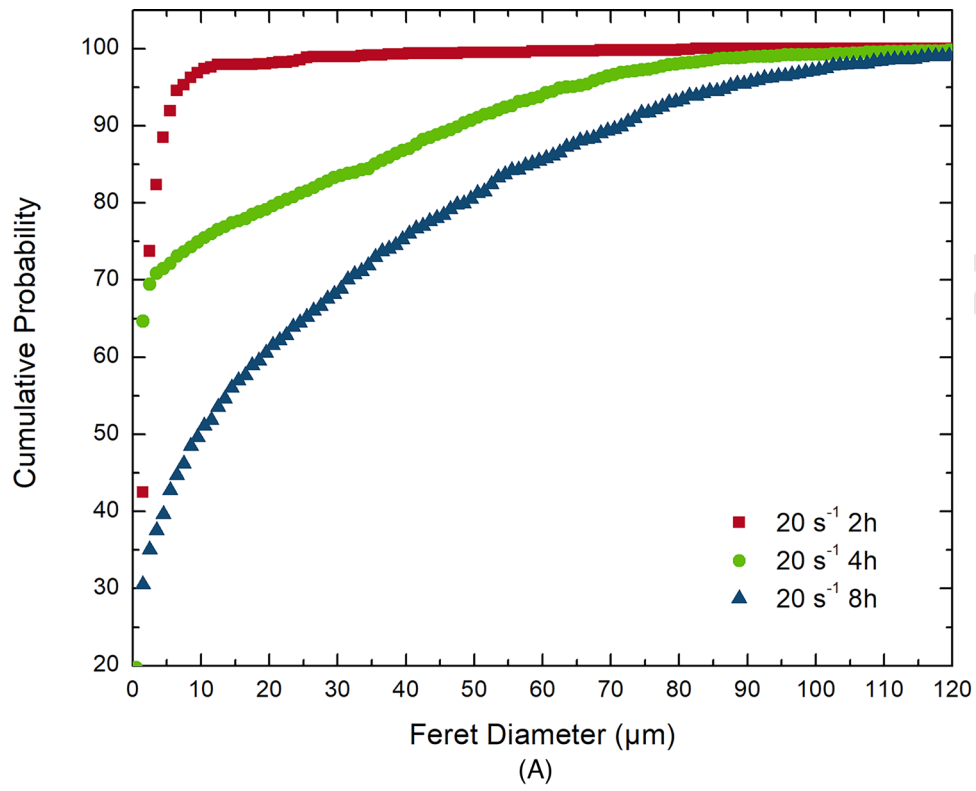


FIGURE 8 Cumulative distribution of the Feret diameter of cerianite crystals for the different experiment durations (A) and conditions of shear rate (B). C10SG glass at 1100°C .

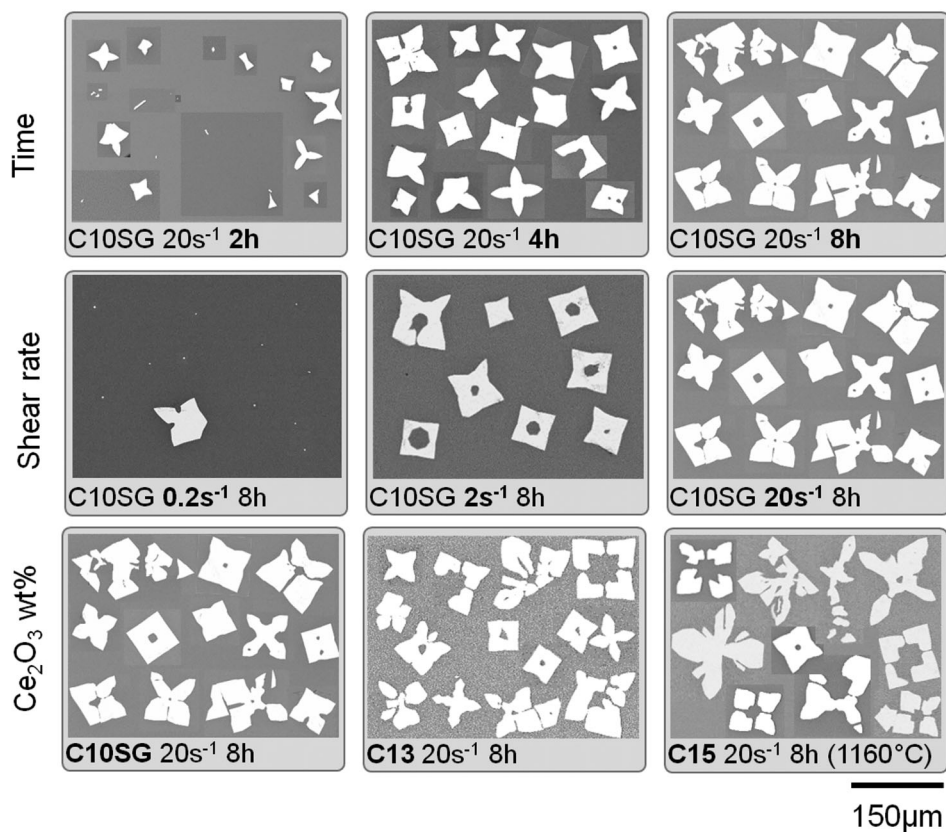


FIGURE 9 Cerianite crystal morphologies for the conditions studied. The images are a mosaic of different crystals in order to make the analysis of the morphology possible and do not represent the real size distributions and densities of the crystals. The 150-µm scale bar is valid for all crystals.

are more energetically favored than smaller ones. This same trend was observed for the conditions with different shear rates, where the condition at 0.2 s^{-1} showed the highest number of crystals for both bulk and surface crystallization. Recent theoretical and experimental studies^{25,32–34,55,56} have suggested that an increase in the stirring speed of melts can in fact increase the crystal nucleation rates. Although our results indicate the opposite trend, this could be a consequence of the Ostwald ripening phenomenon. The N_v for the condition of 0.2 s^{-1} after 8 h observed in Figure 7B is similar to that observed after 2 h (a quarter of the time) of crystallization at 20 s^{-1} , thus suggesting that the nucleation happens faster at higher shear. As indicated by the evolution of the cerianite fraction with time and shear rate in Figure 5B, the cerianite fraction for the condition of 20 s^{-1} after 8 h was higher, which means the crystallization happened faster and is more prone to Ostwald ripening at short times. In other words, our results do not contradict what has been found in recent studies, and indicate that more data on the evolution of N_v with time for the different conditions of shear would help to clarify this hypothesis.

Additionally, based on the morphology of the crystals (dendritic to skeletal), the crystal growth at the conditions studied here is diffusion limited.^{51,53} Under quiescent conditions, as a crystal grows within the melt the region around it becomes chemically impoverished, hindering growth. When a solution is stirred, the size of this impoverished region is expected to decrease, and consequently the growth rate increases. In the case of crystals nucleated in the bulk, both the mean Feret diameter and the crystal size distribution curves show an increase in crystal size with shear rate. For the crystals nucleated at the surface, this phenomenon is even more visible. Based on the size of the biggest crystals, the growth rate estimated for the crystals nucleated at the surface for the conditions of 0.2, 2, and 20 s^{-1} are 3, 9, and 47 µm.h^{-1} , respectively.

Particularly in the case of cerianite crystals, the evolution of the redox equilibrium of cerium in the glass melt is another factor that may affect its kinetics of crystallization. It is well known that the ratio $\text{Ce}^{4+}/(\text{Ce}^{3+} + \text{Ce}^{4+})$ increases as the temperature of the melt decreases,⁵⁷ which could decrease the solubility of the total cerium in the melt,⁴³ that is, favour the precipitation of cerianite.

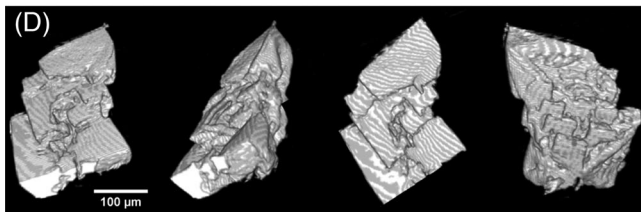
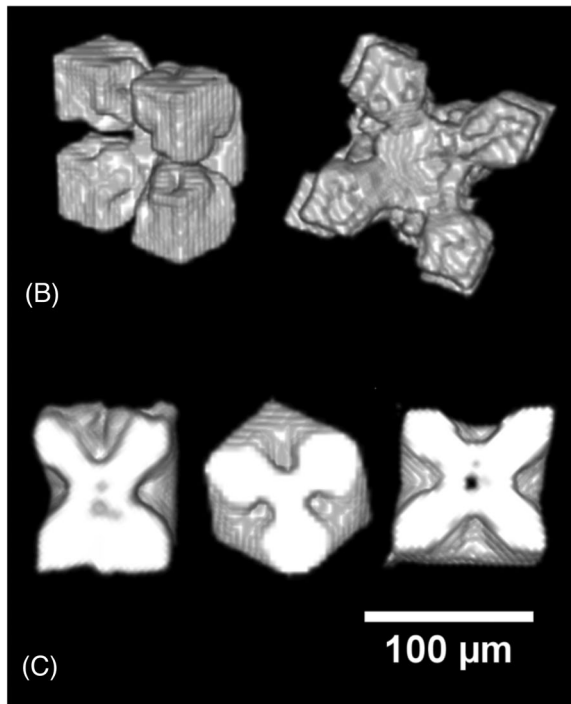
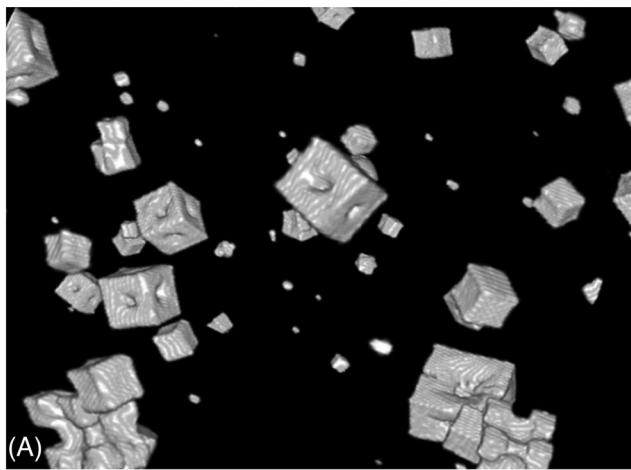
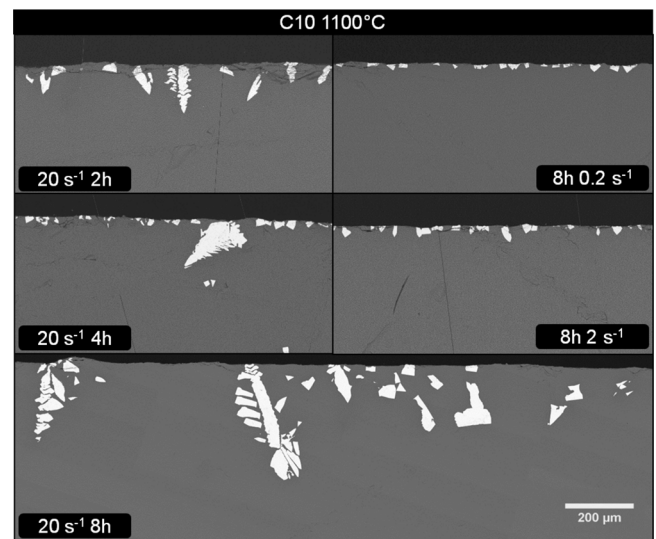
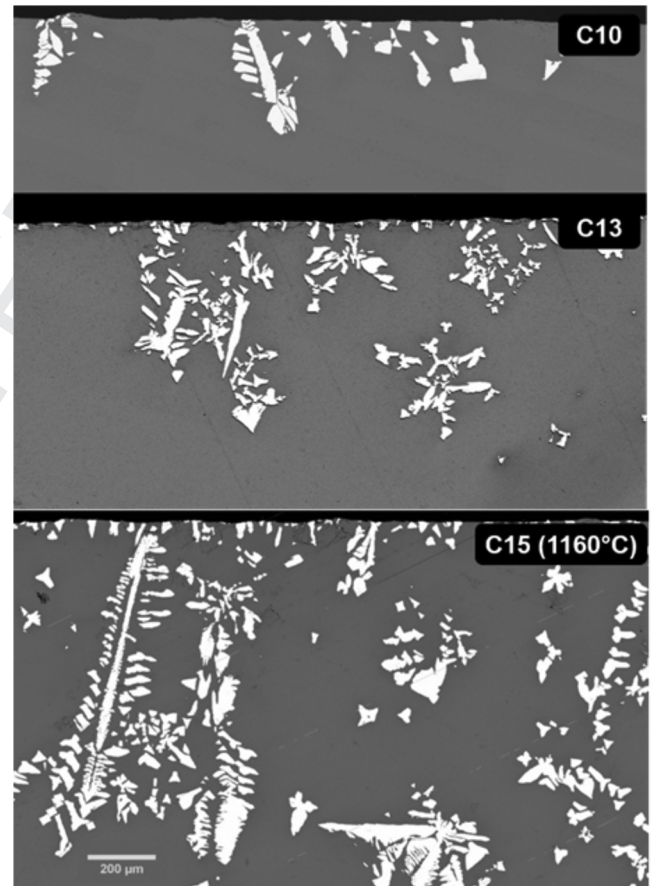


FIGURE 10 3D views reconstructed from X-ray microtomography images: (A) Crystals dispersed in the glass matrix; (B) crystals showing an octapod morphology found in the bulk; (C) different planes of the hollow cubic crystals and (D) 3D views of one of the crystals from the surface of the crucible showing a ripe dendritic morphology. Condition 5 (C10SG, 8 h, and 20 s^{-1}).



(A)



(B)

FIGURE 11 Scanning electron microscopy (SEM) images of the cerianite layer crystallized on the surface of the crucible wall for the different conditions of the experiments. (A) Different conditions of crystallization for the C10SG glass and (B) crystallization at 20 s^{-1} for 8 h for the C10SG, C13, and C15 glasses. All experiments were performed at 1100°C , except for C15, performed at 1160°C .

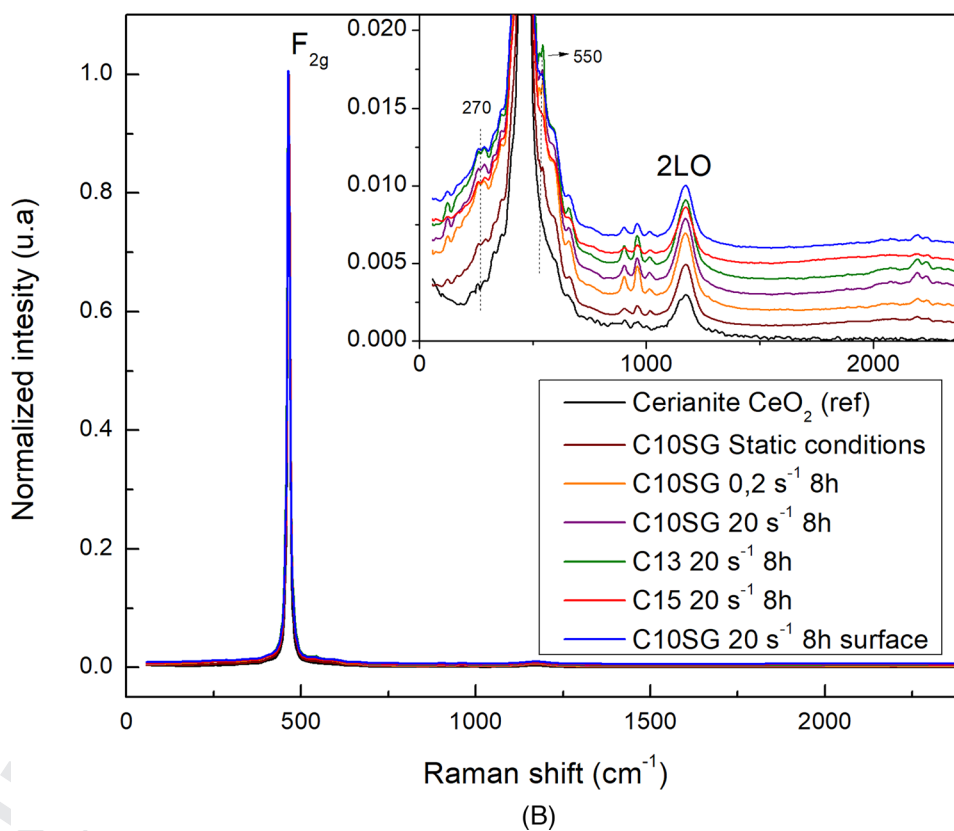
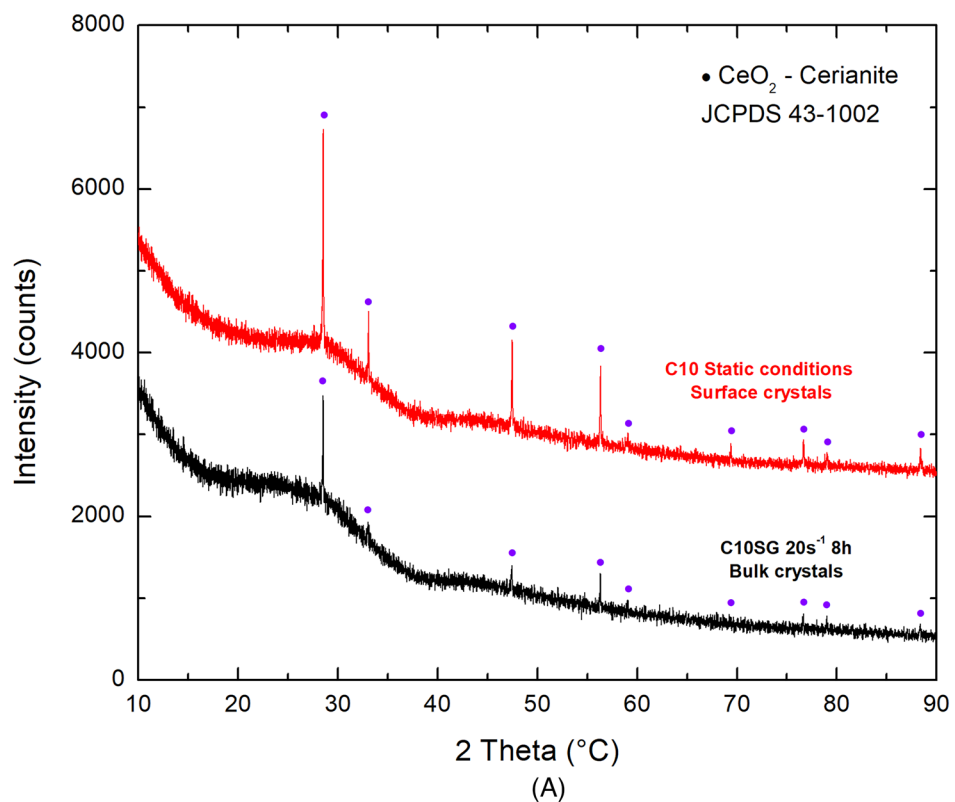


FIGURE 12 (A) XRD plots of the samples collected from the surface and from the bulk. See text for more details. (B) Raman spectra of crystals precipitated under the different conditions studied in this work.

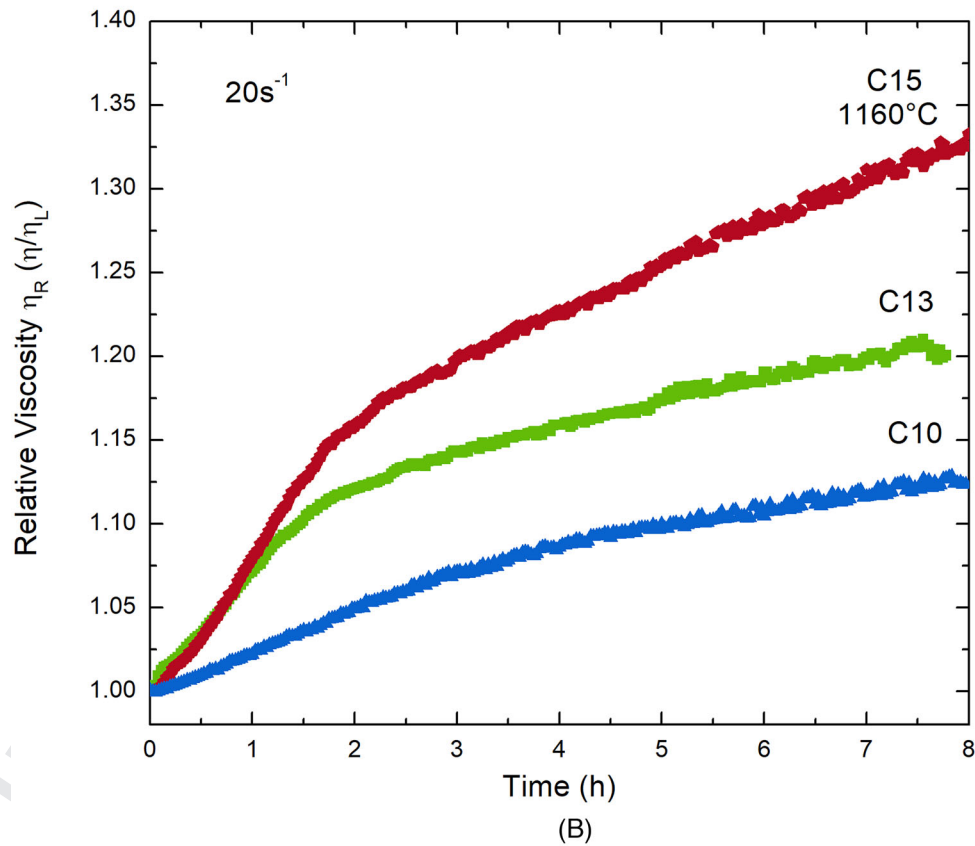
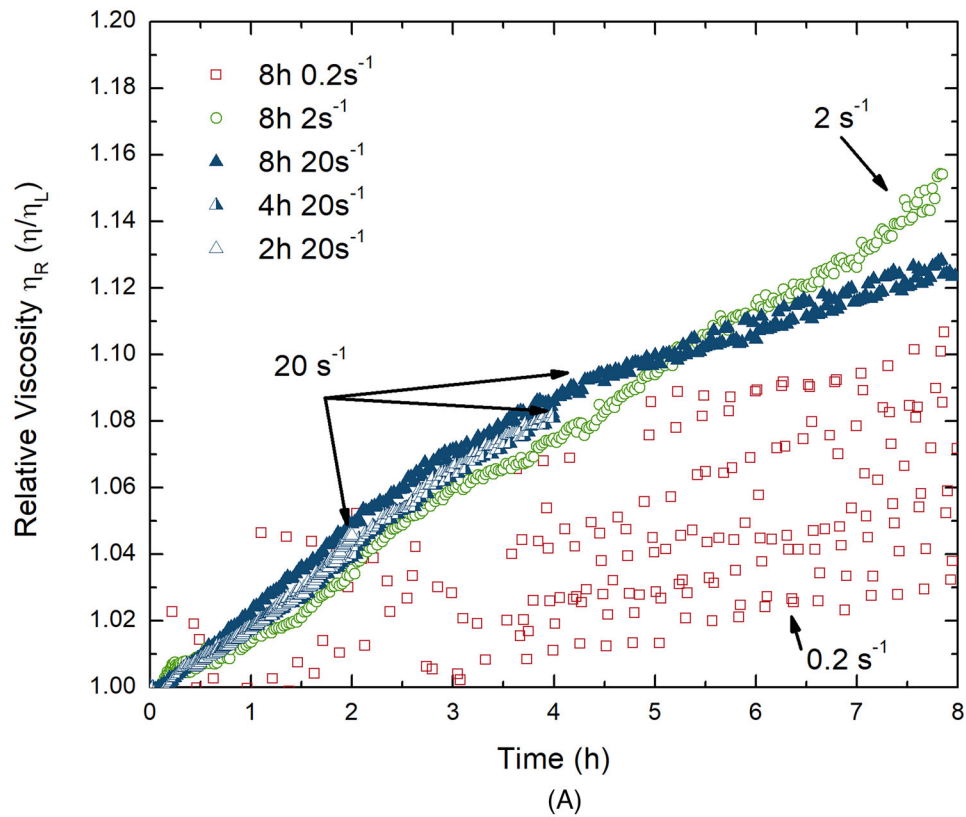


FIGURE 13 Evolution of relative viscosity $\eta_R = \eta/\eta_L$, where η_L is the viscosity of the liquid at the beginning of the experiment. (A) Different conditions of shear for the C10SG glass, and (B) at 20 s^{-1} for the C10SG, C13, and C15 glasses. The experiments were done at 1100°C , except for the C15 glass (1160°C). The viscosity at $\dot{\gamma} = 0.2\text{ s}^{-1}$ shows a fluctuation due to rotor oscillations, and are noticeable only for slow stirring.

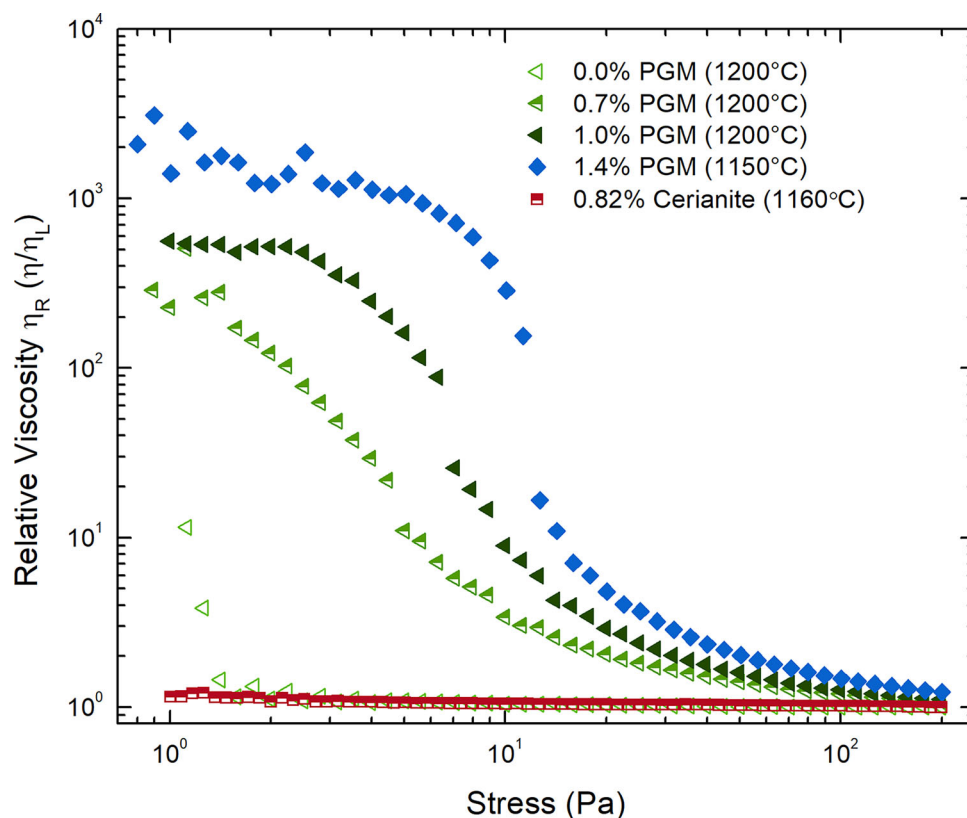


FIGURE 14 Evolution of the relative viscosity with the shear stress (τ) for a glass containing 0.82 vol% of cerianite compared to results for glasses containing PGM particle fractions between 0 and 1.4 vol% studied previously.^{10,11}

Because the thermal treatments were performed at temperatures lower than the elaboration temperature, and the kinetics of the redox reaction are diffusion-controlled, higher shear rates could induce the melt to reach its redox equilibrium at shorter times, and therefore accelerate the precipitation of cerianite.⁵⁸ Nevertheless, the conclusions regarding the effect of shear on the crystallization kinetics of cerianite remain unchanged.

Regarding condition 5 (C10SG – 1100°C-20 s⁻¹-8 h), the crystals that grew on the surface of the crucible reached a significantly bigger size (370 μm) than those in the bulk (maximum size \sim 120 μm). As mentioned earlier, the crystallization experiment was done in a virtual Couette cell, which implies an intrinsic relationship with the concentric cylinder geometry. A special feature of this type of geometry is that the shear rate is not homogeneous in the gap between the cylinders.^{36,59} Considering that the Couette analogy implies a virtual inner cylinder (the rotor) and the outer cylinder (the crucible) to determine the calibration factors, a speed gradient is also present in the gap. Therefore, unlike the crystals in the bulk that are transported together with the melt, the crystals growing on the surface of the crucible are fixed and submitted to stronger convection,^{60,61} and there is probably a higher amount of Ce₂O₃ available to be attached in the growing

crystals. Regarding their morphology, the sections shown in Figure 10C evidence an initial dendritic crystal that changes towards a cubic shape due to the decrease in the supersaturation of the melt (decrease in the Ce₂O₃%). This morphology is also an indication that the system approaches equilibrium.

In the case of the different Ce₂O₃ concentrations, the bigger crystals in the bulk (Figure 6) and on the surface of the crucible of the samples C13 and C15 compared to the C10SG glass can be explained by the higher degree of supersaturation. However in the case of the C15 glass, it might also be related to the higher temperature of crystallization imposed (in order to access the cerianite-only domain), as the kinetics of diffusion accelerate at higher temperatures. The classical dendritic morphologies observed for the C13 and C15 glasses (especially those nucleated on the surface of the crucible), which show a higher degree of branching when compared to the crystals developed in the C10SG glass, are linked to the higher degree of supersaturation. As the driving force for crystallization is higher in these glasses, the morphology is expected to shift towards dendrites, and the degree of branching also increases. This could be an indication that if highly branched dendrites (which could lead to a more pronounced effect on the rheology of the melt, for example due to the higher aspect

ratio) need to be avoided, the Ce_2O_3 wt% has to be limited. Nonetheless, the morphology of crystals is very sensitive to solvent,⁶² so the aforementioned might not be true if the melt is considerably different chemically.

Based on some previous studies [31]–[33] and according to the growth theory,⁶³ a strong enough convection could induce a more euhedral morphology for which a maximal growth rate is displayed. The conditions used in this work did not permit any observation of such a phenomenon, as for all conditions dendritic crystals (more or less ripened) appeared and, thus, supersaturation seems to be the only factor controlling their morphology. Perhaps if higher shear rates had been used, this phenomenon would be visible, but there are equipment limitations at high temperatures due to the low viscosity of the melt.

Furthermore, the XRD and Raman analyses showed no difference between the cerianite crystals precipitated in the different conditions, indicating that the shear conditions do not affect the crystal chemistry.

4.2 | Rheological behavior

The viscosity increase caused by the presence of dispersed particles in suspension in the melt can be estimated by different models proposed in the literature.^{64–69} An estimation using Quemada's model⁶⁹ and considering 1 vol% of monodispersed spherical particles⁷⁰ (a fair approximation for cubic particles^{71,72}) would result in a 3% increase in viscosity. The fact that the viscosity increase observed was superior to the estimated value, and that both 2 and 20 s^{-1} conditions of shear showed similar behavior, even though the resulting cerianite fraction was significantly different, indicate that something other than crystallization is contributing to the phenomenon. One of the reasons for this increase could be the evolution of the redox equilibrium of cerium. It is possible that it causes an effect similar to that observed for glasses containing iron, where the oxidation of the network modifier Fe^{2+} to the network former Fe^{3+} leads to an increase in the viscosity.³⁴ Because the glasses were elaborated at higher temperatures, at the temperatures of crystallization used in this study (1100 and 1160°C) part of the cerium will oxidize ($\text{Ce}^{3+} \rightarrow \text{Ce}^{4+}$).⁴³ As Ce^{4+} leads to a more compact glass structure,⁴⁰ an increase in the viscosity could occur. Another possible reason (perhaps occurring simultaneously) is the evaporation of B_2O_3 and Na_2O during the experiment. In Figure 15, we show the evolution of the $\text{Na}_2\text{O}/\text{SiO}_2$ and $\text{B}_2\text{O}_3/\text{SiO}_2$ ratio (in weight %) in the C10SG glass matrix with time and shear rate. The oxide/ SiO_2 ratio allows an accurate comparison, because the consumption of Ce_2O_3 due to crystallization can mask the evolution of the Na_2O and B_2O_3 contents, and SiO_2 is much less susceptible to evaporation. The evo-

lution of the $\text{Ce}_2\text{O}_3/\text{SiO}_2$ is also shown to evidence the ongoing crystallization.

Figure 15A shows that the evaporation of Na_2O and B_2O_3 occurred mainly in the first 2 h of the experiment, and then this rate reduced. Such behavior could be linked to the steeper increase in viscosity in the first hours of the experiment. Figure 15B shows that for the conditions of 2 and 20 s^{-1} , the B_2O_3 and Na_2O contents were the same, suggesting they underwent the same degree of evaporation, and which could explain the same increase in viscosity observed in Figure 13A. The B_2O_3 content was slightly higher for the 0.2 s^{-1} condition, which indicates that evaporation was less significant for this sample.

When comparing the viscosity change for the different compositions in Figure 13B, we can observe that the increase took place with two different slopes for conditions C13 and C15: a steeper increase during the first 2 h of the experiment, followed by a more moderate slope. After this, the slope shown by the C13 and C10SG glass are the same. However for the experiment with C15 (at a higher temperature), there is a more pronounced slope, backing the evaporation hypothesis as the kinetics of evaporation increase with temperature. The formation of the crystal layer on the surface of the crucible, more accentuated for C13 and C15 glasses, may also play a role in the viscosity measured, but its effect cannot be estimated.

In summary, no significant change in relative viscosity was observed for any of the conditions. The greatest change was observed for the C15 glass (Figure 13B), which reached an η_R of 1.35 after 8 h. The gross increase for this condition was from 9.2 to 12.3 Pa.s, which is negligible in the context of the vitrification process.⁷³ The results suggest that the increase in viscosity was mainly due to evaporation, as only an increase of about 3% would be expected due to crystallization.

In a comparison of the viscosity versus shear behaviors for a PGM-bearing melt and the cerianite-bearing melt, the differences between them can be explained by the distinct morphology and nature of cerianite and PGM particles. While cerianite has a cubic shape, Platinum Group Metal particles have acicular and spherical shapes (RuO_2 needles and PdTe intermetallic spherical beads), and they are frequently found aggregated in small units of about 50 μm ,⁷ even at high shear. The PGM particles' strong interactions engender the formation of bigger aggregates (reaching up to 500 μm ¹³) in the melt when submitted to low shear stress. Both the aggregation and the acicular shape of RuO_2 particles are assumed to be responsible for the critical stress and viscosity augmentation observed in PGM-bearing melts.¹¹

Compared to PGM particles, the chemical nature of cerianite particles is much more similar to that of the melt, and cerianite presents itself as nearly cubic crystals (with some

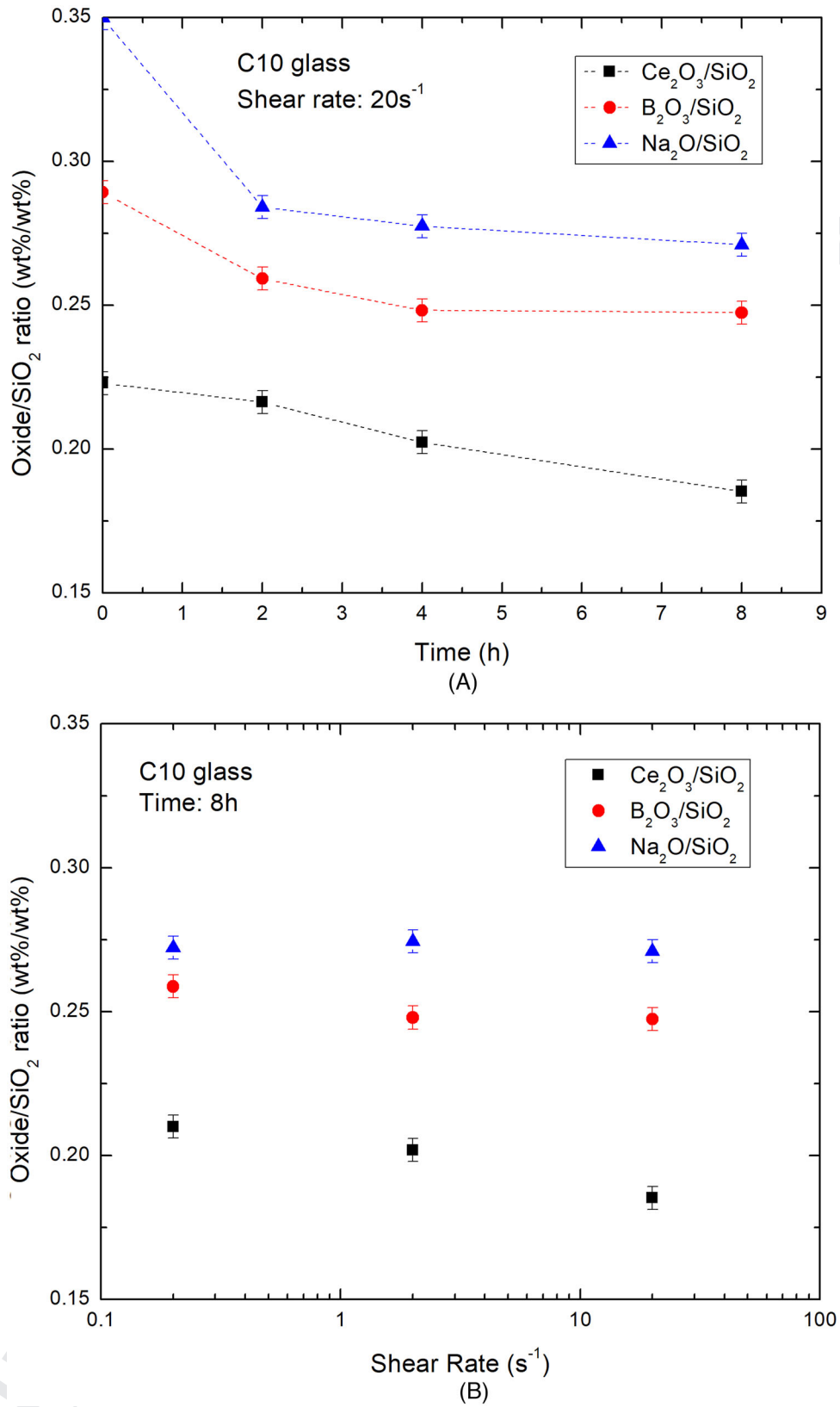


FIGURE 15 Evolution of the oxide/SiO₂ ratio with (A) time and (B) shear rate for the conditions of crystallization with the C10SG glass. T = 1100°C.

overgrown to form dendritic crystals). A study carried out by Saar et al.⁷⁴ estimated the critical crystal fraction (Φ_c) needed for particle percolation (that promotes yield stress) to occur for different particle shapes in crystal-bearing melts. They found that for more equant shapes (spherical or cubic), this critical fraction is higher than for oblate and prolate particles, and according to their study particle percolation of cubic crystals is expected to occur from $\Phi_c = 0.22$ (particle volume of 22%). Therefore, the Newtonian behavior of the cerianite particle fraction studied here could be expected. The non-equant cerianite crystal morphology reported in the previous section for high levels of supersaturation could strongly decrease Φ_c , but this critical fraction could not be assessed due to the high solubility of Ce_2O_3 in the melt. To summarize, our results show that such a small cerianite crystal fraction will not affect the operation of the vitrification process due to viscosity changes.⁷³ A study on the settling of cerianite crystals in static and dynamic conditions would be the next step to verify its effect on the process.

5 | CONCLUSIONS

This work studied the effect of temperature, Ce_2O_3 weight content, and shear rate on the crystallization of a simulated nuclear glass enriched with Ce_2O_3 . The increase in Ce_2O_3 increases the liquidus temperature of the melt, stabilizing the cerianite phase at typical waste vitrification temperatures (above 1000°C) from about 8 wt% of Ce_2O_3 . This increase in Ce_2O_3 content also shifted the apatite domain to higher temperatures, meaning that a significant increase in Ce_2O_3 content could also stabilize apatite at the vitrification temperature.

Based on both static and dynamic experiments, it can be seen that cerianite is prone to show heterogeneous nucleation, and both its morphology and fraction depend upon the Ce_2O_3 wt% and shear conditions. Cerianite crystallization kinetics were slow for all conditions studied. Even for a Ce_2O_3 content as high as 10 wt%, the cerianite fraction after 8 h of crystallization at 1100°C (the approximate vitrification temperature in the hot crucible melter) was less than 1 vol%. Nevertheless, the kinetics were accelerated as the applied shear was augmented. The increase in the Ce_2O_3 wt% led to higher cerianite fractions and to the precipitation of highly-branched dendritic crystals, reaching a length of 1 mm. No significant increment in viscosity due to the crystallization of cerianite was observed for the conditions studied.

For 15 wt% Ce_2O_3 glass compositions, a fraction of 0.8 vol% (in bulk) of cerianite was obtained, but such a particle fraction did not show any effect on the rheology of the melt. This result differs significantly from what has been

observed for PGM particles. The results can be explained by the different nature and morphology of the particles. A study on sedimentation and aggregation phenomena is still needed to completely understand the effect of cerianite on the vitrification process.

ACKNOWLEDGMENTS

The authors would like to thank Emmanuelle BRACKX (CEA-Marcoule) for the microprobe analyses, Sylvain MURE (CEA-Marcoule) for his invaluable support for the rheological measurements, and our Orano and EDF partners for financial support.

ORCID

J. Jiusti  <https://orcid.org/0000-0001-9923-2503>

REFERENCES

1. Vernaz É, Bruezière J. History of nuclear waste glass in France. *Procedia Mater Sci.* 2014;7:3–9.
2. Didierlaurent R, Prevost T, Hugon I, Lemonnier S, Girold C, Maneglia F, et al. Applicability evaluation of the in-can vitrification process to Fukushima waste. In: *Proceedings of the 27th international conference on nuclear engineering (ICONE-27)*; 2019; Japan.
3. Toshiro O, Yasutomo T, Takeshi M, Toyonobu N, Toshiki F. Applicability of vitrification technology for secondary waste generated from contaminated water treatment systems at Fukushima Daiichi nuclear power station. *IHI Eng Rev.* 2020;53(1):7.
4. Vienna JD. Nuclear waste vitrification in the United States: recent developments and future options. *Int J Appl Glass Sci.* 2010;1(3):309–21.
5. Riley BJ, Hrma PR, Vienna JD, Schweiger MJ, Rodriguez CP, Crum JV, et al. The liquidus temperature of nuclear waste glasses: an international round-robin study. *Int J Appl Glass Sci.* 2011;2(4):321–33.
6. Matyáš J, Vienna JD, Peeler DK, Fox KM, Herman CC. Road map for development of crystal-tolerant high level waste glasses. 2014. Accessed May 11, 2021. Available from: <https://www.osti.gov/biblio/1133389>
7. Krause Ch, Luckscheiter B. Properties and behavior of the platinum group metals in the glass resulting from the vitrification of simulated nuclear fuel reprocessing waste. *J Mater Res.* 1991;6(12):2535–46.
8. Simonnet C, Grandjean A, Phalippou J. Electrical behavior of platinum-group metals in glass-forming oxide melts. *J Nucl Mater.* 2005;336(2):243–50.
9. Puig J, Penelon B, Marchal P, Neyret M. Rheological properties of nuclear glass melt containing platinum group metals. *Procedia Mater Sci.* 2014;7:156–62.
10. Hanotin C, Puig J, Neyret M, Marchal P. Platinum group metal particles aggregation in nuclear glass melts under the effect of temperature. *J Nucl Mater.* 2016;477:102–9.
11. Puig J, Hanotin C, Neyret M, Marchal P. High temperature rheological study of borosilicate glasses containing platinum group metal particles by means of a mixer-type rheometer. *J Nucl Mater.* 2016;469:112–9.

12. Nuernberg RB, Machado NMP, Jouglard D, del Campo L, Malki M, Neyret M. The origin of hysteresis in the electrical behavior of RuO₂-glass composite melts. *J Non-Cryst Solids*. 2021;557:120596.
13. Pereira Machado NM, Pereira L, Neyret M, Lemaître C, Marchal P. Influence of platinum group metal particle aggregation on the rheological behavior of a glass melt. *J Nucl Mater*. 2022;563:153618.
14. Avrami M. Kinetics of phase change. I General theory. *J Chem Phys*. 1939;7(12):1103–12.
15. Alton J, Plaisted TJ, Hrma P. The kinetics of Al–Si spinel phase crystallization from calcined kaolin. *J Solid State Chem*. 2010;183(11):2565–9.
16. Hrma P. Crystallization during processing of nuclear waste glass. *J Non-Cryst Solids*. 2010;356(52):3019–25.
17. Orlhac X, Fillet C, Phalippou J. Study of crystallization mechanisms in the French nuclear waste glass. *MRS Online Proc Libr*. 1999;556(1):263.
18. Delattre O, Régnier E, Schuller S, Allix M, Matzen G. Image analysis study of crystallization in two glass compositions of nuclear interest. *J Non-Cryst Solids*. 2013;379:112–22.
19. Levine IN. *Physical chemistry*. 6th ed. New York: McGraw-Hill; 2009.
20. Ferro P, Bonollo F, Timelli G. Sigma phase precipitation modelling in a UNS S32760 superduplex stainless steel. *Metall Ital*. 2012;140:7–12.
21. Fournier J, Régnier E, Faure F, Le Goff X, Brau HP, Brackx E, et al. Application of the JMAK model for crystal dissolution kinetics in a borosilicate melt. *J Non-Cryst Solids*. 2018;489:77–83.
22. Fournier J, Régnier E, Faure F, Le Goff X, Brau HP, Brackx E, et al. Modeling of dissolution kinetics of rare earth crystals in a borosilicate glass melt. *J Non-Cryst Solids*. 2018;481:248–53.
23. Allen RJ, Valeriani C, Tănase-Nicola S, ten Wolde PR, Frenkel D. Homogeneous nucleation under shear in a two-dimensional Ising model: cluster growth, coalescence, and breakup. *J Chem Phys*. 2008;129(13):134704.
24. Lander B, Seifert U, Speck T. Crystallization in a sheared colloidal suspension. *J Chem Phys*. 2013;138(22):224907.
25. Richard D, Speck T. The role of shear in crystallization kinetics: from suppression to enhancement. *Sci Rep*. 2015;5(1):14610.
26. Shao Z, Singer JP, Liu Y, Liu Z, Li H, Gopinadhan M, et al. Shear accelerated crystallization in a supercooled atomic liquid. 2015. Accessed May 30, 2022. Available from: <http://arxiv.org/abs/1407.2078>
27. Mura F, Zaccone A. Effects of shear flow on phase nucleation and crystallization. *Phys Rev E*. 2016;93:042803.
28. Peng HL, Herlach DM, Voigtmann T. Crystal growth in fluid flow: nonlinear response effects. *Phys Rev Materials*. 2017;1(3):030401.
29. Luo S, Li C, Li F, Wang J, Li Z. Ice crystallization in shear flows. *J Phys Chem C*. 2019;123:21042–9.
30. Richard D. Classical nucleation theory for the crystallization kinetics in sheared liquids. *Phys Rev E*. 2019;99:062801
31. Goswami A, Dalal IS, Singh JK. Seeding method for ice nucleation under shear. *J Chem Phys*. 2020;153(9):094502.
32. Goswami A, Dalal IS, Singh JK. Universal nucleation behavior of sheared systems. *Phys Rev Lett*. 2021;126(19):195702.
33. Kouchi A, Tsuchiyama A, Sunagawa I. Effect of stirring on crystallization kinetics of basalt: texture and element partitioning. *Contr Mineral and Petrol*. 1986;93(4):429–38.
34. Chevrel MO, Cimarelli C, deBiasi L, Hanson JB, Lavallée Y, Arzilli F, et al. Viscosity measurements of crystallizing andesite from Tungurahua volcano (Ecuador). *Geochem Geophys Geosyst*. 2015;16(3):870–89.
35. Kolzenburg S, Giordano D, Hess KU, Dingwell DB. Shear rate-dependent disequilibrium rheology and dynamics of basalt solidification. *Geophys Res Lett*. 2018;45(13):6466–75.
36. Aït-Kadi A, Marchal P, Choplin L, Chrissemant AS, Bousmina M. Quantitative analysis of mixer-type rheometers using the couette analogy. *Can J Chem Eng*. 2002;80(6):1166–74.
37. Underwood EE. Stereology, or the quantitative evaluation of microstructures. *J Microsc*. 1969;89(2):161–80.
38. Kilbourn BT. Cerium: a guide to its role in chemical technology. White Plains, NY: Molycorp, Inc.
39. Mansour E. Structure and electrical conductivity of new Li₂O–CeO₂–B₂O₃ glasses. *J Non-Cryst Solids*. 2011;357(5):1364–9.
40. Wang Z, Cheng L. Structural evolution of CeO₂-doped alkali borosilicate glass and the correlation with physical properties based on a revised structural parameter analysis. *RSC Adv*. 2016;6(7):5456–65.
41. Delattre O, Régnier E, Schuller S, Poissonnet S, Massoni N, Allix M, et al. Crystallization kinetics of apatite and powellite in a borosilicate glass under thermal gradient conditions. *Phys Procedia*. 2013;48:3–9.
42. Abdelouas A, Crovisier JL, Lutze W, Grambow B, Dran JC, Müller R. Surface layers on a borosilicate nuclear waste glass corroded in MgCl₂ solution. *J Nucl Mater*. 1997;240(2):100–11.
43. Cachia JN, Deschanel X, Den Auwer C, Pinet O, Phalippou J, Hennig C, et al. Enhancing cerium and plutonium solubility by reduction in borosilicate glass. *J Nucl Mater*. 2006;352(1–3):182–9.
44. Hammer JE, Rutherford MJ. An experimental study of the kinetics of decompression-induced crystallization in silicic melt: kinetics of decompression-induced crystallization. *J Geophys Res*. 2002;107(B1):ECV 8-1-ECV 8-24.
45. Couch S, Harford CL, Sparks RSJ, Carroll MR. Experimental constraints on the conditions of formation of highly calcic plagioclase microlites at the Soufrière Hills Volcano, Montserrat. 2003;44(8):21.
46. Loridant S. Raman spectroscopy as a powerful tool to characterize ceria-based catalysts. *Catal Today*. 2021;373:98–111.
47. Machado NMP. Rheological study of nuclear glass melts containing platinum group metals aggregates bibliographic report. 2020 p. 77.
48. Zanotto ED, James PF. Experimental tests of the classical nucleation theory for glasses. *J Non-Cryst Solids*. 1985;74:373–94.
49. Uhlmann DR. Crystallization and melting in glass forming systems. In: *Kinetics of Reactions in Ionic Systems Proceedings of an International Symposium on Special Topics in Ceramics*; June 18–23, 1967; Alfred, New York.
50. Kirkpatrick RJ, Kuo LC, Melchior J. Crystal growth in incongruently-melting compositions: programmed cooling experiments with diopside. *Am Mineral*. 1981;66(3–4):223–41.
51. Sunagawa I. Characteristics of crystal growth in nature as seen from the morphology of mineral crystals. *Bull Minéral*. 1981;104:81–7.

52. Faure F, Trolliard G, Nicollet C, Montel JM. A developmental model of olivine morphology as a function of the cooling rate and the degree of undercooling. *Contrib Mineral Petrol.* 2003;145(2):251–63.
53. Berg WF. Crystal growth from solutions. *Proc R Soc A.* 1938;164. <https://doi.org/10.1098/rspa.1938.0006>
54. Garcia-Ruiz J, Otolara F. *Crystal Growth in Geology: Patterns on the Rocks. Handbook of Crystal Growth.* Amsterdam, Netherlands: Elsevier; 2015. p. 1–43.
55. Goswami A. Homogeneous nucleation of sheared liquids: advances and insights from simulations and theory. *Phys Chem Chem Phys.* 2021.
56. Campagnola S, Vona A, Romano C, Giordano G. Crystallization kinetics and rheology of leucite-bearing tephriphonolite magmas from the Colli Albani volcano (Italy). *Chem Geol.* 2016;424:12–29.
57. Pinet O, Hugon I, Mure S. Redox control of nuclear glass. *Procedia Mater Sci.* 2014;7:124–30.
58. Schreiber HD. Redox processes in glass-forming melts. *J Non-Cryst Solids.* 1986;84(1):129–41.
59. Dou HS, Khoo BC, Yeo KS. Instability of Taylor–Couette flow between concentric rotating cylinders. *Int J Therm Sci.* 2008;47(11):1422–35.
60. Barresi AA, Marchisio D, Baldi G. On the role of micro- and mesomixing in a continuous Couette-type precipitator. *Chem Eng Sci.* 1999;54(13–14):2339–49.
61. Abou-Ziyan H, Ameen R, Elsayed K. Fluid flow and convection heat transfer in concentric and eccentric cylindrical annuli of different radii ratios for Taylor–Couette–Poiseuille flow. *Adv Mech Eng.* 2021;13(8):16878140211040732.
62. Zhao X, Bao Z, Sun C, Xue D. Polymorphology formation of Cu₂O: a microscopic understanding of single crystal growth from both thermodynamic and kinetic models. *J Cryst Growth.* 2009;311(3):711–5.
63. Dhanaraj G, Byrappa K, Prasad V, Dudley M. *Springer handbook of crystal growth.* Berlin, Heidelberg: Springer Berlin Heidelberg; 2010. Available from: <http://link.springer.com/10.1007/978-3-540-74761-1>
64. Einstein A. Eine neue bestimmung der moleküldimensionen. *Ann Phys.* 1906;324(2):289–306.
65. Vand V. Viscosity of solutions and suspensions. I. Theory. *J Phys Chem.* 1948;52(2):277–99.
66. Mooney M. The viscosity of a concentrated suspension of spherical particles. *J Colloid Sci.* 1951;6(2):162–70.
67. Krieger IM, Maron SH. Rheology of synthetic latex. I. Test of some flow equations. *J Colloid Sci.* 1951;6(6):528–38.
68. Roscoe R. The viscosity of suspensions of rigid spheres. *Br J Appl Phys.* 1952;3:267–9.
69. Daniel Quemada. *Modélisation rhéologique structurelle.* Paris: Lavoisier; 2006.
70. Mueller S, Llewellyn EW, Mader HM. The rheology of suspensions of solid particles. *Proc R Soc A.* 2010;466(2116):1201–28.
71. Cwalina CD, Harrison KJ, Wagner NJ. Rheology of cubic particles suspended in a Newtonian fluid. *Soft Matter.* 2016;12(20):4654–65.
72. Vetere F, Iezzi G, Perugini D, Holtz F. Rheological changes in melts and magmas induced by crystallization and strain rate. *C R Géosci.* 2022;354(S1):1–22.
73. Advocat T, Dussossoy JL, Petitjean V. *Vitrification des déchets radioactifs. Verres et céramiques.* 2008. Accessed June 20, 2022. Available from: <https://www.techniques-ingenieur.fr/doi/10.51257/a/v1/bn3664>
74. Saar MO, Manga M, Cashman KV, Fremouw S. Numerical models of the onset of yield strength in crystal–melt suspensions. *Earth Planet Sci Lett.* 2001;187(3):367–79.

SUPPORTING INFORMATION

Additional supporting information can be found online in the Supporting Information section at the end of this article.

How to cite this article: Jiusti J, Regnier E, Machado NMP, Ghazzai M-L, Malivert V, Neyret M, et al. Precipitation of cerianite crystals and its effect on the rheology of a simplified nuclear glass melt. *Int J Appl Glass Sci.* 2023;1–23. <https://doi.org/10.1111/ijag.16639>